Contrasted porosity between the hanging-wall and the footwall of the active Pāpaku thrust at IODP Site U1518: insights on deformation and erosion history and sediment compaction state evolution during accretion at the northern Hikurangi margin deformation front

Jade Dutilleul[a]*, S. Bourlange[a] and Y. Géraud[a]

[a]*University of Lorraine, CNRS, GeoRessources, F-54000 Nancy, France*

*jade.dutilleul@univ-lorraine.fr

Abstract

Attempts to determine physical property across thrust faults at subduction zones through drilling, logging and core sampling have been limited and restricted to exhumed accretionary prisms or shallow parts of active wedges. However, characterizing porosity evolution across the sedimentary section entering subduction zones and accreted sediments is crucial to understand deformation history at accretionary margins through determination of sediment trajectories, quantification of transported volumes of sediments and fluids with related mechanical responses and understanding deformation processes in and around fault zones. International Ocean Discovery Program Expeditions 372 and 375 drilled, logged and cored the entering basin (Site U1520) and active Pāpaku thrust (Site U1518) few kilometers landward of the northern Hikurangi margin deformation front where tsunami earthquakes and recurrent slow slip events occur. Here, we examine physical properties evolution across the Pāpaku thrust at Site U1518 including geophysical logging data, pore size distribution obtained by combining Nuclear Magnetic Resonance and Mercury Injection Capillary Pressure, and interstitial porosity that is representative of sediment compaction state, and compare with that of Site U1520. Interstitial porosity is determined by correcting total connected porosity

from clay-bound water content based on cation exchange capacity. We evidence strong variations of physical properties across the thrust fault, with lower porosity, higher P-wave velocity and resistivity in the hanging-wall than in the footwall. We suggest that the porosity pattern at the Pāpaku thrust evidences differences in maximum burial depth with an overcompacted hanging-wall that has been uplifted, thrusted and concomitantly eroded above a nearly normally consolidated younger footwall.

1. Introduction

Over the last two decades, strong research effort focused on better understanding how the shallow part of subduction zones accommodates displacement by hosting a wide variety of slip modes like tsunami earthquakes (e.g Bilek and Lay, 2002; Seno, 2002; Dean et al., 2010; Geersen et al., 2013), afterslip and coseismic slip (e.g. Chlieh et al., 2007), slow slip events (e.g. Liu & Rice 2007; Bell et al., 2010; Basset et al., 2014; Kodaira et al., 2004; Wallace and Beavan, 2006, 2010; Song et al., 2009; Saffer and Wallace, 2015; Wallace et al., 2004, 2009, 2012, 2016), steady creep (e.g. Wang and Bilek, 2014), tectonic tremor (e.g. Shelly et al., 2006) and (very-)low-frequency-earthquakes (e.g. Ito and Obara, 2006). Recently, IODP Expeditions 372 and 375 provided in situ data to investigate the physical processes thought to trigger spatial and temporal transitions between fault slip styles by drilling several sites across the northern Hikurangi margin, in an area offshore Gisborne where Pacific plate is obliquely subducted beneath the Australian Plate at ~5.0 cm/y (Fig. 1a) (Wallace et al., 2004). There, tsunami earthquakes nucleate (Doser and Webb, 2003) and slow slip events recur down to 2km below the seafloor (Fig. 1b), potentially propagating to the trench along the plate interface and/or splay faults within the prism (Saffer et al., 2019; Fagereng et al., 2019; Shaddox and Schwartz, 2019; Mouslopoulou et al., 2019). Site U1520 was

logged and cored in the basin entering the margin ~95 km from shore and ~16 km oceanward of the deformation front (Fig.1b,c) so that the initial lithological, physical, hydrological and thermal properties of the input section could be characterized (Dutilleul et al., in press). This site revealed a very heterogeneous input section composed by a Quaternary to Paleocene sedimentary cover with siliciclastic trench sediments (Units I-III) overlying pelagic carbonate formations (Unit IV), above Cretaceous-aged volcaniclastic Units V-VI of the subducting Hikurangi Plateau (Barnes et al., 2019; Barnes et al., 2020). Landward, in the frontal wedge ~6.5 km west of the deformation front, Site U1518 penetrated an active thrust fault, the Pāpaku fault, its hanging-wall and uppermost footwall up to ~492 meters below sea floor (mbsf) (Saffer et al., 2019). The Pāpaku fault, intersected at ~304 mbsf, is a <30° westward-dipping splay fault which is thought to lie in the SSE rupture area, to host SSEs and to have accommodated several kilometers of shortening within the prism (Fagereng et al., 2019). The hanging-wall corresponds to lithologic Unit I (0-~304 mbsf) with Early-Mid Pleistocene (>0.53 Ma) hemipelagic silty-claystone and fine-grained turbidites sequences. It is folded with bedding dips ranging 0-50°, faulted and pervasively fractured up to 100m above the Pāpaku fault zone (Fig. 2h). The Pāpaku thrust fault zone mainly corresponds to lithologic Unit II (~304-370 mbsf; <0.53 Ma) with hemipelagic mudstone alternating with thin and sparse layers of silty mudstone to sandy siltstone. It is composed of a ~18m-thick main fault zone (MFZ, Fig. 2a) characterized by a mixture of brittle (breccia, faults and fractures) and ductile (flow bands) structures, with ductile features locally overprinted by faults and fractures (Fagereng et al., 2019). Below, there are a ~21m-thick zone of gradually decreasing deformation intensity where structures are more ductile than brittle, and a ~10m-thick subsidiary fault zone. No significant change in lithology occurs in the footwall. It is mainly composed by

relatively undeformed Mid-Late Pleistocene (<0.53 Ma) Unit III (~370-492 mbsf) bioturbated hemipelagic mudstones with turbidites sequences, few ductile-flow deformation structures and occasional faults.

Here, we characterize the evolution of bound water content, pore structure and interstitial porosity across the Pāpaku thrust at Site U1518. Although porosity is dependent on numerous parameters like lithology, mineralogy, grain size or sedimentation rates, we assume that the Quaternary siliciclastic trench sediments forming the hanging-wall, the fault zone and the upper footwall at Site U1518 can be correlated to undeformed Hikurangi Trough siliciclastic Units I-III at reference Site U1520 (base SU4 and SU5, Fig. 1) based on seismic correlation (Barnes et al., 2020). We compare interstitial porosity and pore structure data at both sites to assess how accretion and thrusting affects sediment physical properties at Site U1518 and get insights on deformation history at the deformation front. Following previous works (Henry, 1997; Henry and Bourlange, 2004; Conin et al., 2011; Dutilleul et al., 2020 and in press), we determine interstitial porosity that is representative of the compaction state at Site U1518 by correcting total connected porosity (equivalent to onboard MAD porosity in Wallace et al., 2019) from clay-bound water content using post-cruise geochemical data like Cation Exchange Capacity (CEC) and exchangeable cation composition. We further characterize the evolution of pore geometry and size with increasing depth by combining Mercury Injection Capillary Pressure (MICP) and Nuclear Magnetic Resonance (NMR), which yield a different range of information.

2. Materials and methods

2.1. Sampling and data

Our study is based on 1) onboard data including geophysical logging data and

measurements on core samples and 2) post-cruise analysis of 52 core samples with commonly one sample per core (approximately 1 sample each 10 meter). Samples were picked up as close as possible from the samples that were squeezed onboard for interstitial water composition analysis. They were shipped and stored at chilled temperature (2-8°C) in sealed plastic bags with a sponge saturated with seawater to preserve moisture. Comparison of onboard and post-cruise total connected porosity measurement evidence that moisture was successfully preserved. Porosity data measured on samples were correlated to logging-while-drilling (LWD) neutron and NMR porosity data.

2.2 Methods

2.2.1 Quantification of porosity

2.2.1.1. Estimation of bound water content and interstitial porosity from CEC, soluble chloride content and interstitial water composition

Total connected porosity was measured according to Blum's (1994) onboard procedure that consists in measuring the mass of the sample when it's wet (m_{wet}) and it's mass (m_{dry}) and volume (V_{dry}, measured using a Micromeritics® AccuPyc II 1340 helium-displacement pycnometer) after a 24-hours stage of drying in a convection oven at 105°C±5°C to remove both interstitial and clay bound water. Interstitial water corresponds to the chloride-bearing water located in the pore space that is expellable by compaction-induced dewatering as sediments are buried. Clay bound water includes chloride-free water located in the interlayer space and electrostatically bound on particle surfaces because of the compensation of negatively charged layers by hydrated cations. It is generally poorly affected by compaction (e.g. Bird 1984; Colten-Bradley, 1987; Fitts and Brown, 1999; Henry and Bourlange, 2004; Dutilleul et al., 2020) and

transiently released when sediments reach the smectite dehydration to illite pressure-temperature (<150°C) window. The calculation of total connected porosity ϕ_t and grain density ρ_g is corrected for the precipitation of salt during drying:

$$\phi_t = \frac{V_f}{V_{wet}} = \frac{V_f}{V_f + V_{dry} - V_{salt}} \quad \text{and} \quad \rho_g = \frac{m_s}{V_s}$$

where $V_f = \frac{m_f}{\rho_f}$ is the volume of pore fluid with $m_f = \frac{m_w}{1-s}$ the pore fluid mass, $m_w = m_{wet} - m_{dry}$ the pore water mass, s the salinity (0.035) and ρ_f the density of pore fluid (1.024 g/cm3), $V_{salt} = \frac{m_{salt}}{\rho_{salt}} = \frac{m_w\ s}{(1-s)\ \rho_{salt}}$ is the salt volume with m_{salt} the salt mass and ρ_{salt} the density of salt (2.220g/cm3), $m_s = m_{wet} - m_f = m_{dry} - m_{salt}$ is the mass of solids excluding salt and $V_s = V_{dry} - V_{salt}$ the volume of solids excluding salt.

Dry samples were then ground using a Retsch® mixer mill MM200 with agate grinding beads and jars. Chemical analyses including cation exchange capacity (CEC) measured by exchange with cobaltihexamine and ultraviolet-visible spectrometer Varian SpectrAA 800 Zeeman, exchangeable cation composition (Na+, K+, Ca2+ and Mg2+) measured by atomic absorption spectrometer Thermo Scientific ICE 3300 and soluble chloride content per dry mass determined by sequential water extraction (Tessier et al., 1979) and ion chromatography were carried on at the Laboratoire Interdisciplinaire des Environnements Continentaux (LIEC) in Nancy and Metz, France.

Interstitial porosity (ϕ_i) and bound water content (ϕ_b) were determined from the total connected porosity (ϕ_t), n the average number of water molecules per cation charge (n=15 is used corresponding to smectites with two layers of water following Dutilleul et al., in press and Fig. 3), M_w the water molar mass (M_w = 0.018kg/mol), the density of pore fluid ρ_f, the grain density ρ_g and the CEC:

$$\phi_i = \phi_t - \phi_b = \phi_t - n \frac{M_w}{\rho_f} CEC \rho_g (1 - \phi_t)$$

We express pore volume loss at specific depth as:

$$\frac{\Delta V}{V_o} = \frac{(\phi_{i0} - \phi_i)}{(1 - \phi_i)}$$

with ΔV the volume loss, V_o the initial volume and ϕ_{i0} the initial interstitial porosity (Saito and Goldberg,1997)

2.2.1.2. Resistivity-derived porosity

We determined resistivity-derived porosity from resistivity logs at Site U1518 using Revil et al. (1998)'s resistivity model for clay-rich materials with high surface conductivity σ_s. This model is based on Archie's law (Archie, 1942) that links the resistivity-derived porosity ϕ to the formation factor $F = a\,\phi^{-m}$ where m and a are constants. Previous works have shown that resistivity-derived porosity determined using this model with a =1 and a cementation factor 1≤ m ≤3.5 fits interstitial porosity (Conin et al., 2011; Dutilleul et al., in press) in siliciclastic clay-rich materials. Assuming Bussian (1983) and Bourlange et al. (2003)'s hypotheses since $\frac{\sigma_s}{\sigma_{if}} \ll 1$ at Site U1518, F can be expressed:

$$F = \frac{\sigma_{if}}{\sigma} \left[1 + 2 \frac{\sigma_s}{\sigma_{if}} \left(\frac{\sigma_{if}}{\sigma} - 1 \right) \right]$$

The conductivity of the interstitial fluid σ_{if} is determined from the concentration of Cl-, Na^+, K^+, Ca^{2+}, Mg^{2+} and SO_4^{2-} in interstitial water (C_{iws}^i) and seawater (C_{sw}^i), the ionic mobility in the fluid β_f^i and Z_i the number of charges of ions given by Revil et al. (1998), and σ_{sw} the sea water conductivity:

$$\sigma_{if} = \sigma_{sw} \frac{\sum_i \left(\beta_f^i \times Z_i \times C_{iws}^i \right)}{\sum_j \left(\beta_f^j \times Z_j \times C_{sw}^j \right)}$$

with $\sigma_{sw} = 5.32(1 + 0.02(T - 25))$ and $T(°C) = 1.64 + 35.0 \times 10^{-3} z$ at Site U1518 (Saffer et al., 2019).

σ_s is calculated assuming a major contribution of the Stern layer to surface electrical conduction, spherical grains and a linear temperature dependency of the exchangeable cation mobility β_s:

$$\sigma_s = \frac{2}{3} \rho_g \, CEC \, \beta_s$$

2.2.2. Pore-network characterization

Mercury Injection Capillary Pressure (MICP) and Nuclear Magnetic Resonnance (NMR) were performed on 14 samples to characterize macro- (>50 nm) to mesopore (2-50 nm) size distribution (e.g. Dutilleul et al., in press) according to the IUPAC nomenclature (Sing et al., 1985) and pore geometry evolution.

2.2.2.1. ***Mercury Injection Capillary Pressure (MICP)***

MICP was performed at room temperature (20°C) using a Micromeritics® AutoPore IV 9500 on samples that were previously oven-dried at 105°C±5°C for 24h. The sample is first degassed under vacuum during the low-pressure analysis before the volume of intruded mercury is gradually measured up to a mercury pressure of ~0.2 MPa. The high-pressure analysis consists in stepwise measurements of the volume of intruded mercury during an intrusion-extrusion-reintrusion cycle providing the size distribution of pore throats but also mercury-trapped porosity that is mercury total connected porosity corrected from mercury-free porosity. During the first intrusion stage, the mercury fills the connected pore space as mercury injection pressure is progressively increased up to 220 MPa. This stage provides mercury-total connected porosity and the

183 distribution of the size of pore throats from 360 μm to 5.7 nm using the Young-Laplace
184 equation:

$$r = \frac{2\,\sigma_{Hg}\cos\theta_{Hg}}{P_{Hg}}$$

185 where r is the pore throat radius (m), σ_{Hg} is the air-mercury interfacial tension (0.485
186 N/m), θ_{Hg} is the mercury-sediment contact angle (140°) and P_{Hg} is the mercury
187 injection pressure (Pa). During the extrusion stage, the pressure is decreased down to
188 atmospheric pressure with some mercury droplets remaining trapped at narrow pore
189 throats (Li and Wardlaw, 1986a, b) allowing to determine the mercury-trapped porosity,
190 an indicator of pore compaction state. Finally, mercury-free porosity only is reintruded
191 as mercury injection pressure is increased up to the maximum value of 220 MPa. The
192 distribution of pore throats size was used to determine permeability K_{KT} using the Katz-
193 Thompson permeability model (Katz and Thompson, 1986,1987; Nishiyama and
194 Yokoyama, 2014):

195 $$K_{KT} = \frac{1}{89}\phi_i \frac{(l^h_{max})^3}{l_c} f(l^h_{max})$$

196 with l_c the pore throat diameter of the inflexion point of the cumulative pore-throat size
197 distribution, l^h_{max} the pore throat diameter corresponding to the optimum path for
198 permeability where the fractional volume of pore diameters of l and larger $f(l^h_{max})$ is
199 maximum.

200 **2.2.2.2.** ***Nuclear Magnetic Resonance (NMR)***

201 NMR measurements were performed using Bruker® Minispec Mq20 at room
202 temperature (20°C) and atmospheric pressure on core samples with a diameter of 8 mm.
203 The transverse relaxation time T_2 was measured using the Carr-Purcell-Meilboom-Gill
204 (CPMG) sequence with a recycle delay of 0.1s and a half-echo time τ of 0.04 ms (the

minimum available for this equipment), a gain ranging 70-80%, 200 echoes per scan and 128 scans were stacked. We used UpenWin© software to inverse the raw T_2 exponential decay in a smoothed T_2 distribution. We correlated the T_2 (msec) measured to MICP pore throat radius (µm) based on ρ_e the effective relaxivity (µm/sec) following Marschall et al. (1995) using the relation:

$$T_2 = \frac{1000r}{2\,\rho_e}$$

We also determined NMR porosity as suggested by Daigle et al. (2014) based on the volume of water V_w in the sample:

$$\phi_{NMR} = \frac{V_w}{V_w + V_s}$$

V_w is determined using a calibration where the maximum signal amplitude A_0 (corrected for the gain) is recorded during the T_2 measurement for known volume of water: V_w=19.762A_0 – 0.092 (R^2=0.94). This method was validated using synthetic samples of known porosity.

3. Results

3.1. Mineralogy and Cation Exchange Capacity (CEC)

Total clay content is relatively homogeneous and elevated (32%-52%, in average ~46%) through Unit I to III with no change from either side of the fault zone (Fig. 2b). Cation exchange capacity is low to intermediate (0.08-0.18 mol/kg, in average 0.15 mol/kg) through the sedimentary section (Fig. 2c). CEC tends to increase with total clay content and shows minimum values in Subunit IIIA contorted domains possibly corresponding to mass transport deposits (MTDs). This range of CEC values suggests that the clay mineral assemblage is mainly composed of kaolinite and/or chlorite and/or illite rather than smectite.

3.2. Physical properties

Overall, onboard total connected porosity averages 43% at Site U1518 but exhibits a large scatter up to 11%. There is a remarkable total connected porosity difference >10% between the hanging-wall and the footwall, with a hanging-wall exhibiting a general trend of lower values compared to the footwall. In both the hanging-wall and the footwall, total connected porosity decreases exponentially with increasing depth z or effective vertical stress σ_v' with similar Archie's law parameters (Table 1). In the hanging-wall, total connected porosity exponentially decreases from ~66% near the seafloor to ~40% at bottom of the Pāpaku main fault zone (Fig. 2d), with Subunit IB showing values that are a few percent higher and that decrease more quickly with increasing depth than in Subunit IA. Across the Pāpaku fault zone, total connected porosity increases up to 54% with wide and reduced scatter in the main and subsidiary fault zones respectively. In the footwall, total connected porosity decreases to 39%, with slightly higher values in Subunit IIIB than IIIA. Although a major transition in porosity occurs at the fault zone, it is possible to fit a single Archie's law across the Pāpaku thrust that is $\phi_t = 44.3e^{-\frac{z}{12937}}$ or $\phi_t = 44.3e^{-0.012\,\sigma_v'}$.

As a result of relatively constant and low CEC values, bound water content is constant and low (3-8%, in average 6%) across the section drilled at Site U1518 (Fig. 2d).

Because of relatively constant bound water content, the evolution of interstitial porosity (Fig. 2d and g) is very similar to that of total connected porosity, showing a ~10% increase through the Pāpaku fault zone and comparable exponential decrease trends with increasing depth in the footwall and the hanging-wall (Table 1). Interstitial porosity decreases in the hanging-wall from 62% to ~33% at the top of the fault zone with a few percent higher values in Subunit IB than IA, increases up to 48% through the fault zone and decreases up to ~33% through the footwall with slightly higher values in

Subunit IIIB than IIIA. Resulting total pore volume loss (Saito and Goldberg, 1997) is twice higher in the hanging-wall (~0.4) than in the footwall (~0.2).

LWD neutron and NMR porosities (Wallace et al., 2019) show a global trend that matches that of total connected and interstitial porosities, with exacerbated porosity contrast between the hanging-wall and the footwall (Fig. 2d). Continuous LWD porosity data are able to record detailed porosity evolution across the Pāpaku fault zone. Both LWD neutron and NMR porosity increase by stages through the main fault zone, the subsidiary fault zone and the zone in between. Overall, LWD neutron porosity satisfying fits to total connected porosity but exhibits higher porosity difference between the hanging-wall and the footwall with values up to 5% higher than measured on samples in the footwall. LWD NMR porosity values are significantly lower than interstitial and total connected porosities, except in Subunit IA where it fits interstitial porosity. It exhibits the highest porosity shift (~20%) through the Pāpaku fault zone. Resistivity-derived porosity can be fitted to interstitial porosity data using m =2.2 in Subunit IA and m =2.7 from Subunit IB to IIIB. The shift toward higher cementation factor values occurs at the coring gap in the hanging-wall that also corresponds to the top of the hanging-wall damage zone.

Overall, LWD resistivity and P-wave velocity are anti-correlated with porosity (Fig. 2f). P-wave velocity (resp. resistivity) increases from ~1550 m/s (resp. ~1.8 ohm/m) at the seafloor to ~2200m/s (resp. ~3.8 ohm/m) at the bottom of the hanging-wall, decreases to ~1700 m/s (resp. ~1.5 ohm/m) across the Pāpaku fault zone and increases up to ~2100 m/s (resp. ~2.4 ohm/m) in the footwall. Within the Pāpaku fault zone, both P-wave velocity and resistivity decrease by stages in the main fault zone, the subsidiary fault zone and in between.

3.3 Pore structure

Overall, MICP and NMR (Fig. 2e) show that samples are macroporous (i.e. pore diameters >50 nm using the nomenclature of Sing et al., 1985) with only one family of pore size that globally decreases and becomes more homogeneous with increasing depth, from ~0.8 µm in average near the seafloor to ~0.2 µm in average in Subunit IIIB, except in the Pāpaku fault zone where it locally increases and becomes more heterogeneous. A slight increase in pore size can also be noticed in Subunit IIIB compared to Subunit IIIA.

At Site U1518, there is no clear relation between interstitial porosity and mean pore throats diameter, mercury porosity or mercury trapped porosity for the hanging-wall, the fault zone and the footwall (Fig. 4). Katz-Thompson permeability decreases with depth from ~$7.25 \cdot 10^{-17}$ m² to ~$1.3 \cdot 10^{-17}$ m² in the hanging-wall, ranges $1.2 \cdot 10^{-17}$-$6.3 \cdot 10^{-18}$ m² in the Pāpaku fault zone and $1.05 \cdot 10^{-16}$-$3.6 \cdot 10^{-17}$ m² in the footwall.

Average NMR T_2 signals follow the same evolution than pore throats size given by MICP, although strong discrepancy occurs between the values measured by the LWD tool and on the samples. T_2 measured on the samples is ~2.8 ms near the seafloor and decreases to ~2 ms in the footwall. LWD NMR T_2 steadily decreases from ~9 ms near the seafloor to ~4 ms at the bottom of the hanging-wall, increases through the Pāpaku fault zone up to 25 ms, and steadily decreases through the footwall to ~7 ms. This discrepancy could be due to a different calibration of the LWD NMR tool (Wallace et al., 2019) compared to laboratory measuring device.

4. Discussion

4.1. Comparison of interstitial porosity and pore structure data of accreted Quaternary siliciclastic sequence at Site U1518 with undeformed sequence at Site U1520

Porosity data in accreted siliciclastic Quaternary sequence at Site U1518 including interstitial porosity data that is representative of the compaction state exhibit contrasted values in the hanging-wall and the footwall of the Pāpaku thrust. If the hanging-wall and the footwall show interstitial porosity values that similarly exponentially decrease with increasing depth (Fig. 2d, g) or effective vertical stress (Table 1), the hanging-wall is characterized by lower values than the footwall, the transition to higher porosity values occurring across the Pāpaku fault zone.

This evolution of interstitial porosity at Site U1518 contrasts with that of the correlated undeformed sequence drilled seaward at Site U1520 (Fig. 1c), that exclusively shows exponential decrease with increasing effective vertical stress following the reference compaction curve $\phi_i = 46.6e^{-0.029\,\sigma_v'}$ (R^2=0.29) from ~66% near the seafloor to 40% at the bottom of siliciclastic Unit III (Fig. 5). This compaction trend is attributed to normal consolidation associated with pre-accretion compaction-induced dewatering that releases interstitial water as the sequence is progressively buried in the basin entering the subduction zone (Bray and Karig, 1985). By comparison, interstitial porosity is more scattered at Site U1518 than at Site U1520. In average, it is ~5-10% lower in the hanging-wall at Site U1518 than the reference U1520 compaction curve at this range of depth. Through the Pāpaku fault zone, interstitial porosity increases up to a range of values close to U1520 compaction curve values at these depths. In the upper section of the footwall drilled at Site U1518, it nearly averages the values of the reference curve or is only few percent lower. The comparison of interstitial porosity data in accreted

siliciclastic Quaternary sequence at Site U1518 with the reference compaction curve determined from correlated undeformed sequence at Site U1520 evidences an overcompacted hanging-wall as mentioned by Fagereng et al. (2019), a normally consolidated Pāpaku fault zone and a slightly overcompacted to nearly normally consolidated upper footwall at Site U1518 (Fig. 5a).

Pore diameter measured by MICP and estimated from NMR measurements on samples and LWD NMR is equivalent at Site U1518 and in Site U1520 siliciclastic units (Fig. 6a), except in the intensively fractured part the hanging-wall >100 mbsf at Site U1518 where it is lower (~0.2 µm) than at equivalent depth at Site U1520 where it averages 0.5 µm (Fig. 6b). T_2 measured on samples and LWD T_2 show similar behaviour (Fig. 6c). Katz-Thompson permeability is also ~1 order of magnitude lower in the hanging-wall at Site U1518 than at equivalent depth at Site U1520 (Fig. 6d). Globally, the trends relating interstitial porosity, mean pore throats diameters, mercury porosity and mercury trapped porosity in undeformed siliciclastic sediments at Site U1520 is suitable for sediments at Site U1518, although these latter mostly correspond to a low porosity-small pores endmember (Fig. 4).

4.2. Insights on compaction state evolution and deformation history of Quaternary siliciclastic sequence during accretion

Progressive burial of unconsolidated sediments deposited in the basin entering subduction zones results in the mechanical compaction of the pore network with continuous release of interstitial water until lithification into rocks (e.g. Bray and Karig, 1985; Fagereng et al., 2018). In drained conditions, compaction-induced dewatering is thus associated with a reduction and homogenization of pore diameters, an exponential decrease of interstitial porosity (vertical loading trend following the normal

consolidation curve $\phi_i = \mathrm{a}e^{-\mathrm{b}\,\sigma'_v}$, Fig. 7) and possibly a reduction of permeability. Tectonic and hydrologic events that commonly occurs in the shallow part of subduction zones deviates interstitial porosity from the normal consolidation trend (Bray and Karig, 1985 and references therein; Saito and Goldberg, 1997; Conin et al., 2011) as detailed in Figure 7.

Based on these theoretical shifts, we propose a simple model where erosion and thrusting are concomitant and potentially associated with excess pore pressure build up and horizontal shortening to explain the interstitial porosity profile observed at Site U1518 (Fig. 8). In the hanging-wall, the interstitial porosity data are significantly lower than the value of the reference compaction curve and can be fitted to the latter assuming a vertical effective stress increase of ~7.5±1.0 MPa corresponding to ~830±110 meters of supplementary burial occurred (Fig. 5b). In the footwall where the data are closer to the reference compaction curve, a lower vertical effective stress increase of ~3.0±1.0 MPa corresponding to ~330±110 meters of supplementary burial has to be assumed. Such stress shifts could be the result of erosion (Fig. 7b).

We suggest that both the hanging-wall and the footwall sequences have experienced vertical loading as they were progressively buried after deposition in the entering basin, resulting in decreasing pore size with increasing depth and in the normal consolidation trends observed (Fig. 7a; 8a). The trends for the hanging-wall and footwall (Table 1) are similar because of analogous lithology in both sequences. Based on stress shift values, we infer that the sequence that will later form the hanging-wall was buried ~830±110 meters deeper than present depth in the entering basin before thrust, thus reaching a maximum thickness of ~1130±110 meters. This estimation is in accordance with the depth at the trench of the base SU4 reflector (Fig. 1c) that approximately corresponds to the base of the hanging-wall at Site U1518. This suggests that the tectonic setting at Site

U1518 before thrust is analogous to present tectonic setting at the trench. This significant thickness is likely to have favoured sediment consolidation and transition to brittle behaviour with faults and fractures development. We explain the stress shift for the footwall showing that the latter was buried ~330±110 meters deeper than present depth by erosion history occurring in at least two main stages in a case of limit scenario. In a first time, ~500 meters of the hanging-wall sequence was eroded as it was thrusted above the footwall (Fig. 8b). In a second time, once the hanging-wall was set above the footwall for a maximum thickness of ~630±110 meters, ~330±110 meters of material was eroded so the hanging-wall reaches its actual thickness of ~300 meters (Fig. 8c). These values represent maximum values assuming perfectly drained conditions and no overcompaction associated with tectonic strain (Fig. 7c). However, it is very likely that these values are overestimated because 1) the hanging-wall may have undergone horizontal shortening as it was folded and thrusted (e.g. Saffer and Tobin, 2011; Hamahashi et al., 2013) and 2) conditions may not have been perfectly drained in the footwall allowing to pore pressure build-up as the hanging-wall was thrusted above it (Fig. 7d). Elevated pore fluid pressure in the footwall is suggested by the injection features observed in intervals showing ductile flow structures (Fagereng et al., 2019). Because of the lower peak P-T conditions experienced by the footwall compared to the hanging-wall, the footwall was likely weaker than the hanging-wall during faulting (Hamashi et al., 2013) and composed by poorly consolidated fluid-rich sediments where excess pore pressure may have developed as a response to the thrusting of the hanging-wall above it. Present interstitial porosity profile in the footwall implies that overpressured fluids were expelled before the second erosion stage, allowing the poorly deformed footwall to consolidate and to develop few brittle deformation structures.

4.3 Comparison with other splay faults

Although limited in situ geophysical or core data are available in clay-rich thrust faults, similar porosity contrasts between the footwall and the hanging-wall have been observed at exhumed (e.g. Hamahashi et al., 2013) and modern splay faults (e.g. Saito and Goldberg, 1997 at Barbados; Bourlange et al., 2003; Conin et al., 2011; Tao and Sen, 2012; Cerchiari et al., 2018 at Nankai), with also higher porosity in the footwall than in the hanging-wall. Overall, this porosity transition across the fault zone evidences difference in maximum burial depth, with uplifted and unroofed overcompacted hanging-wall above younger less consolidated footwall. Overcompaction of the hanging-wall may also be favoured by the thickening of the prism as thrust sheets stack, resulting in horizontal shortening and tectonic compaction (Saito and Goldberg, 1997).

Here, similarly to Conin et al. (2011) and Hamahashi et al. (2013) but contrary to Saito and Goldberg (1997) a unique cementation factor m is required to fit the porosity data across the damage zone of the hanging-wall, the fault zone and the footwall. At the Pāpaku thrust, m is higher but in the range of values that has been previously described at modern splay faults of the Nankai Kumano transect (Conin et al., 2011) or Barbados (Saito and Goldberg, 1997) although the quantitative method used in the latter study is not rigorously based on the same hypotheses. In particular, the lower m value found in the poorly damaged part of the hanging-wall that roughly corresponds to Subunit IA contrasts with the work of Saito and Goldberg (1997) that evidences higher m in the hanging-wall than in the footwall, although a varies. However, it contrasts with the very low values evidenced at exhumed splay faults where porosity decreases (Hamahashi et al., 2013). The unique value of m for the deformed hanging-wall, the fault zone and the footwall may be related to similarities in microstructures and mineralogy in the footwall and the hanging-wall (e.g. Hamahashi et al., 2013) although grain size slightly differs between both.

5. Conclusion

Based on IODP Expeditions 372/375 logging data and samples, we have evidenced strong porosity contrasts between the hanging-wall and the footwall of the active Pāpaku splay fault at northern Hikurangi margin. As observed at exhumed and modern splay faults at different subduction zones, the footwall is characterized by higher porosity values than the hanging-wall that is overconsolidated compared to equivalent normally consolidated siliciclastic input sequence at Site U1520. Resistivity and P-wave velocity exhibit an evolution that is anti-correlated with that of porosity. Based on porosity reversals from the reference compaction curve at Site U1520, we suggest that the hanging-wall underwent pre-accretion consolidation as it was buried in the entering basin in a setting that is similar to that of the actual proto-thrust, before being thrusted above younger and less consolidated sediments of the footwall and unroofed by concomitant erosion. Other processes may have contributed to shift porosity from the reference compaction curve like 1) the build-up of pore pressure in the footwall in case of disequilibrium compaction and 2) poorly drained conditions and folding and thrusting of the hanging-wall associated with horizontal shortening. Overall, the Pāpaku thrust at northern Hikurangi margin exhibits lithological, structural and physical properties similar to that of shallow splay faults in early stage of deformation, although present data do not allow to precisely quantify dewatering and pore pressure.

6. Acknowledgements

We greatly acknowledge the funding of the shore-based measurements of CNRS-INSU and IODP-France. We thank David Billet, Philippe Rousselle, Maximilien Beuret, Géraldine Kitzinger and Hervé Marmier from the LIEC laboratory in Nancy and Metz (France) for running CEC, exchangeable cation composition and soluble chloride content analyses.

7. Data

This research used data provided by the International Ocean Discovery Program (IODP) and freely available on the LIMS Report Interface Page at *web.iodp.tamu.edu/LORE* or on the log database at *mlp.ldeo.columbia.edu/logdb/scientific_ocean_drilling.* Post-cruise data including corrected porosity, CEC, exchangeable cation composition, MICP and NMR are available in the OTELo Research Data Repository (https://doi.org/10.24396/ORDAR-31).

8. References

Archie, G. E. (1942). The electrical resistivity log as an aid in determining some reservoir characteristics, Trans. Am. Inst. Min. Metall. Pet. Eng., 146, 54-62

Barnes, P.M., Wallace, L.M., Saffer, D.M., Pecher, I.A., Petronotis, K.E., LeVay, L.J., Bell, R.E., Crundwell, M.P., Engelmann de Oliveira, C.H., Fagereng, A., Fulton, P.M., Greve, A., Harris, R.N., Hashimoto, Y., Hüpers, A., Ikari, M.J., Ito, Y., Kitajima, H., Kutterolf, S., Lee, H., Li, X., Luo, M., Malie, P.R., Meneghini, F., Morgan, J.K., Noda, A., Rabinowitz, H.S., Savage, H.M., Shepherd, C.L., Shreedharan, S., Solomon, E.A., Underwood, M.B., Wang, M., Woodhouse, A.D., Bourlange, S.M., Brunet, M.M.Y., Cardona, S., Clennell, M.B., Cook, A.E., Dugan, B., Elger, J., Gamboa, D., Georgiopoulou, A., Han, S., Heeschen, K.U., Hu, G., Kim, G.Y., Koge, H., Machado, K.S., McNamara, D.D., Moore, G.F., Mountjoy, J.J., Nole, M.A., Owari, S., Paganoni, M., Rose, P.S., Screaton, E.J., Shankar, U., Torres, M.E., Wang, X., and Wu, H.-Y. (2019). Site U1520. In Wallace, L.M., Saffer, D.M., Barnes, P.M., Pecher, I.A., Petronotis, K.E., LeVay, L.J., and the Expedition 372/375 Scientists, Hikurangi Subduction Margin Coring, Logging, and Observatories. (2019). Proceedings of the

International Ocean Discovery Program, 372B/375: College Station, TX (International Ocean Discovery Program). https://doi.org/10.14379/iodp.proc.372B375.105.2019

Barnes, P.M., Wallace, L.M., Saffer, D.M., Bell, R.E., Underwood, M.B., Fagereng, A., Meneghini, F., Savage, H.M., Rabinowitz, H.S., Morgan, J.K., et al. (2020). Slow slip source characterized by lithological and geometric heterogeneity. Science Advances 6, eaay3314.

Bassett, D., Sutherland, R., and Henrys, S. (2014). Slow wavespeeds and fluid overpressure in a region of shallow geodetic locking and slow slip, Hikurangi subduction margin, New Zealand. Earth and Planetary Science Letters 389, 1–13.

Bell R, Sutherland R, Barker DHN, Henrys S, Bannister S, et al. (2010). Seismic reflection character of the Hikurangi subduction interface, New Zealand, in the region of repeated Gisborne slow slip events. Geophys. J. Int. 180(1):34–48

Bilek, S.L., and Lay, T. (2002). Tsunami earthquakes possibly widespread manifestations of frictional conditional stability: Variability of Greenland accumulation. Geophysical Research Letters 29, 18-1-18–4.

Bird, P. (1984). Laramide crustal thickening event in the Rocky Mountain Foreland and Great Plains: Tectonics, v. 3, no. 7, p. 741–758, doi:10.1029/TC003i007p00741.

Blum, P. (1994). Index properties, vers. 155. In ODP Shipboard laboratory Manual, College Station, TX (Ocean drilling Program).

Bourlange, S., Henry, P., Moore, J.C., Mikada, H., Klaus, A. (2003). Fracture porosity in the décollement zone of Nankai accretionary wedge using Logging while Drilling resistivity data. Earth Planet. Sci. Lett. 209, 103–112. https://doi.org/10.1016/S0012-821X(03)00082-7.

491 Bray, C. J. and Karig, D. E. (1985). Porosity of sediments in accretionary prisms and
492 some implications for dewatering processes, J. Geophys. Res., 90, 768–778,
493 https://doi.org/10.1029/JB090iB01p00768
494 Bussian, A.E., (1983). Electrical conductance in a porous medium. Geophysics 48 (9),
495 1258–1268. https://doi.org/10.1190/1.1441549.

496 Cerchiari, A., Fukuchi, R., Gao, B., Hsiung, K.-H., Jaeger, D., Kaneki, S., Keller, J.,
497 Kimura, G., Kuo, S.-T., Lymer, G., et al. (2018). IODP workshop: Core-Log Seismic
498 Investigation at Sea – Integrating legacy data to address outstanding research questions
499 in the Nankai Trough Seismogenic Zone Experiment. Scientific Drilling 24, 93–107.

500 Chlieh, M., Avouac, J.-P., Hjorleifsdottir, V., Song, T.-R.A., Ji, C., Sieh, K., Sladen, A.,
501 Hebert, H., Prawirodirdjo, L., Bock, Y., et al. (2007). Coseismic Slip and Afterslip of
502 the Great Mw 9.15 Sumatra-Andaman Earthquake of 2004. Bulletin of the
503 Seismological Society of America 97, S152–S173.

504 Conin, M., Henry, P., Bourlange, S., Raimbourg, H., and Reuschlé, T. (2011).
505 Interpretation of porosity and LWD resistivity from the Nankai accretionary wedge in
506 light of clay physicochemical properties: Evidence for erosion and local overpressuring:
507 Porosity and LWD resistivity from Nankai. Geochemistry, Geophysics, Geosystems 12.

508 Colten-Bradley, V.A. (1987). Role of pressure in smectite dehydration - effects on
509 geopressure and smectite-to-illite transformation, AAPG Bull. 71, 1414-1427.

510 Daigle, H., Thomas, B., Rowe, H., and Nieto, M. (2014). Nuclear magnetic resonance
511 characterization of shallow marine sediments from the Nankai Trough, Integrated
512 Ocean Drilling Program Expedition 333: NMR of Nankai Trough sediments. Journal of
513 Geophysical Research: Solid Earth 119, 2631–2650.

514 Dean, S.M., McNeill, L.C., Henstock, T.J., Bull, J.M., Gulick, S.P.S., Austin, J.A.,
515 Bangs, N.L.B., Djajadihardja, Y.S., and Permana, H. (2010). Contrasting Décollement
516 and Prism Properties over the Sumatra 2004-2005 Earthquake Rupture Boundary.
517 Science 329, 207–210.

518 Doser, D.I., and Webb, T.H. (2003). Source parameters of large historical (1917-1961)
519 earthquakes, North Island, New Zealand. Geophysical Journal International 152, 795–
520 832.

521 Dutilleul, J., Bourlange, S., Conin, M., and Géraud, Y. (2020). Quantification of bound
522 water content, interstitial porosity and fracture porosity in the sediments entering the
523 North Sumatra subduction zone from Cation Exchange Capacity and IODP Expedition
524 362 resistivity data. Marine and Petroleum Geology 111, 156–165.

525 Fagereng, Å, Diener, J.F.A., Ellis, S., and Remitti, F. (2018). Fluid-related deformation
526 processes at the up- and downdip limits of the subduction thrust seismogenic zone:
527 What do the rocks tell us?, in Byrne, T., Underwood, M.B., Fisher, D., McNeill, L.,
528 Saffer, D., Ujiie, K., and Yamaguchi, A., eds., Geology and Tectonics of Subduction
529 Zones: A Tribute to Gaku Kimura: Geological Society of America Special Paper 534, p.
530 187–215, https://doi.org/10.1130/2018.2534(12).

531 Fagereng, Å., Savage, H.M., Morgan, J.K., Wang, M., Meneghini, F., Barnes, P.M.,
532 Bell, R., Kitajima, H., McNamara, D.D., Saffer, D.M., et al. (2019). Mixed deformation
533 styles observed on a shallow subduction thrust, Hikurangi margin, New Zealand. 47, 6.

534 Fitts, T.G. and Brown, K.M. (1999). Stress-induced smectite dehydration: ramifications
535 for patterns of freshening and fluid expulsion in the N. Barbados accretionary wedge,
536 Earth Planet. Sci. Lett. 172, 179-197.

537 Geersen, J., McNeill, L., Henstock, T.J., and Gaedicke, C. (2013). The 2004 Aceh-
538 Andaman Earthquake: Early clay dehydration controls shallow seismic rupture: Shallow
539 Rupture off Northern Sumatra. Geochemistry, Geophysics, Geosystems 14, 3315–3323.

540 Hamahashi, M., Saito, S., Kimura, G., Yamaguchi, A., Fukuchi, R., Kameda, J.,
541 Hamada, Y., Kitamura, Y., Fujimoto, K., Hashimoto, Y., et al. (2013). Contrasts in
542 physical properties between the hanging wall and footwall of an exhumed seismogenic
543 megasplay fault in a subduction zone-An example from the Nobeoka Thrust Drilling
544 Project: physical property of exhumed splay fault. Geochemistry, Geophysics,
545 Geosystems 14, 5354–5370.

546 Henry, P. (1997). Relationship between porosity, electrical conductivity and cation
547 exchange capacity in Barbados wedge sediments, Proc. Ocean Drill. Program Sci.
548 Results, 156, 137–149

549 Henry, P., Bourlange, S., (2004). Smectite and fluid budget at Nankai IODP sites
550 derived from cation exchange capacity. Earth Planet. Sci. Lett. 219, 129–145.
551 https://doi. org/10.1016/S0012- 821X(03)00694-0.

552 Ito, Y., Obara, K. (2006). Very low frequency earthquakes within accretionary prisms
553 are very low stress-drop earthquakes. Geophys. Res. Lett. 33:L09302

554 Katz, A.J., and Thompson, A.H. (1986). Quantitative prediction of permeability in
555 porous rock. Physical Review B 34, 8179–8181.

556 Katz, A.J., and Thompson, A.H. (1987). Prediction of rock electrical conductivity from
557 mercury injection measurements. Journal of Geophysical Research 92, 599.

Kodaira, S., Iidaka, T., Kato, A., Park, J.-O., Iwasaki, T., and Kaneda, Y. (2004) High pore fluid pressure may cause silent slip in the Nankai Trough: Science, v. 304, p. 1295–1298, https://doi.org/10.1126 /science.1096535.

Li, Y. and N.C., Wardlaw (1986a). The influence of wettability and critical pore throat size ratio on snap-off, Journal of Colloid and Interface Science, 109(2), 461-472

Li, Y. and N.C., Wardlaw (1986b). Mechanisms of nonwetting phase trapping during imbibition at slow rates, Journal of Colloid and Interface Science, 109(2), 473-486

Liu, Y., and Rice, J.R. (2007). Spontaneous and triggered aseismic deformation transients in a subduction fault model. Journal of Geophysical Research 112.

Marschall, D., Gardner, J.S., Mardon, D., and Coates, R. (1995). Method for Correlating NMR Relaxometry and Mercury injection Data. 12.

Mouslopoulou, V., Saltogianni, V., Nicol, A., Oncken, O., Begg, J., Babeyko, A., Cesca, S., and Moreno, M. (2019). Breaking a subduction-termination from top to bottom: The large 2016 Kaikōura Earthquake, New Zealand. Earth and Planetary Science Letters 506, 221–230.

Nishiyama, N., and Yokoyama, T. (2014). Estimation of permeability of sedimentary rocks by applying water-expulsion porosimetry to Katz and Thompson model. Engineering Geology 177, 75–82.

Revil, A., Cathles III, L. M., Losh, S. and Nunn, J. A. (1998). Electrical conductivity in shaly sands with geophysical applications, J. Geophys. Res., 103, 23,925–23,936, doi:10.1029/98JB02125.

579 Saffer, D.M., and Tobin, H.J. (2011). Hydrogeology and Mechanics of Subduction Zone
580 Forearcs: Fluid Flow and Pore Pressure. Annual Review of Earth and Planetary
581 Sciences 39, 157–186.

582 Saffer, D.M., and Wallace, L.M. (2015). The frictional, hydrologic, metamorphic and
583 thermal habitat of shallow slow earthquakes: Nature Geoscience, v. 8, p. 594–600,
584 https://doi.org/10.1038/ngeo2490.

585 Saffer, D.M., Wallace, L.M., Barnes, P.M., Pecher, I.A., Petronotis, K.E., LeVay, L.J.,
586 Bell, R.E., Crundwell, M.P., Engelmann de Oliveira, C.H., Fagereng, A., Fulton, P.M.,
587 Greve, A., Harris, R.N., Hashimoto, Y., Hüpers, A., Ikari, M.J., Ito, Y., Kitajima, H.,
588 Kutterolf, S., Lee, H., Li, X., Luo, M., Malie, P.R., Meneghini, F., Morgan, J.K., Noda,
589 A., Rabinowitz, H.S., Savage, H.M., Shepherd, C.L., Shreedharan, S., Solomon, E.A.,
590 Underwood, M.B., Wang, M., Woodhouse, A.D., Bourlange, S.M., Brunet, M.M.Y.,
591 Cardona, S., Clennell, M.B., Cook, A.E., Dugan, B., Elger, J., Gamboa, D.,
592 Georgiopoulou, A., Han, S., Heeschen, K.U., Hu, G., Kim, G.Y., Koge, H., Machado,
593 K.S., McNamara, D.D., Moore, G.F., Mountjoy, J.J., Nole, M.A., Owari, S., Paganoni,
594 M., Rose, P.S., Screaton, E.J., Shankar, U., Torres, M.E., Wang, X., and Wu, H.-Y.
595 (2019). Expedition 372B/375 summary. In Wallace, L.M., Saffer, D.M., Barnes, P.M.,
596 Pecher, I.A., Petronotis, K.E., LeVay, L.J., and the Expedition 372/375 Scientists,
597 Hikurangi Subduction Margin Coring, Logging, and Observatories. Proceedings of the
598 International Ocean Discovery Program, 372B/375: College Station, TX (International
599 Ocean Discovery Program). https://doi.org/10.14379/iodp.proc.372B375.101.2019

600 Shaddox, H.R., and Schwartz, S.Y. (2019). Subducted seamount diverts shallow slow
601 slip to the forearc of the northern Hikurangi subduction zone, New Zealand. Geology
602 47, 415–418.

603 Saito, S., and Goldberg, D. (1997). Evolution of tectonic compaction in the Barbados
604 accretionary prism: Estimates from logging-while-drilling. Earth and Planetary Science
605 Letters 148, 423–432.

606 Shelly, D. R., Beroza, G.C., Iden S., Nakamura, S. (2006). Low frequency earthquakes
607 in Shikoku, Japan, and their relationship to episodic tremor and slip. Nature 442:188–91

608 Seno, T. (2002). Tsunami earthquakes as transient phenomena. Geophysical Research
609 Letters 29, 58-1-58–4.

610 Sing, K.S., Everett, D.H., Haul, R.A.W., Moscou, L., Pierotti, R.A., Rouquerol, J.,
611 Siemieniewsha, T., (1985). Reporting physisorption data for gas/solid systems with
612 special reference to the determination of surface area and porosity. Pure Appl. Chem.
613 57, 603e619.

614 Song, T.A., Helmberger, D.V., Brudzinski, M.R., Clayton, R.W., Davis, P., et al.
615 (2009). Subducting slab ultra-slow velocity layer coincident with silent earthquakes in
616 southern Mexico. Science 324:502–6

617 Tao, Y., and Sen, M.K. (2012). Shallow splay fault properties of the Nankai Trough
618 accretionary wedge inferred from seismic inversion. Journal of Geophysics and Engineering
619 9, 1–11.

620 Wallace, L.M., Beavan, J., McCaffrey, R., and Desmond, D. (2004). Subduction zone
621 coupling and tectonic block rotations in the North Island, New Zealand. Journal of
622 Geophysical Research 109.

623 Wallace, L. M., & Beavan, J. (2006). A large slow slip event on the central Hikurangi
624 subduction interface beneath the Manawatu region, North Island, New Zealand.
625 Geophysical Research Letters, 33(11).

626 Wallace, L. M., Reyners, M., Cochran, U., Bannister, S., Barnes, P. M., Berryman, K., et al.
627 (2009). Characterizing the seismogenic zone of a major plate boundary subduction thrust:
628 Hikurangi Margin, New Zealand. Geochemistry, Geophysics, Geosystems, 10(10).

629 Wallace, L. M., & Beavan, J. (2010). Diverse slow slip behavior at the Hikurangi
630 subduction margin, New Zealand. Journal of Geophysical Research: Solid Earth, 115(B12).

631 Wallace, L. M., Beavan, J., Bannister, S., Williams, C. (2012). Simultaneous long-term
632 and short-term slow slip events at the Hikurangi subduction margin, New Zealand:
633 Implications for processes that control slow slip event occurrence, duration, and
634 migration. J. Geophys. Res. 117, B11402.

635 Wallace, L. M., Webb, S. C., Ito, Y., Mochizuki, K., Hino, R., Henrys, S., et al. (2016).
636 Slow slip near the trench at the Hikurangi subduction zone, New Zealand. *Science*,
637 *352*(6286), 701-704.

638 Wallace, L.M., Saffer, D.M., Barnes, P.M., Pecher, I.A., Petronotis, K.E., LeVay, L.J.,
639 Bell, R.E., Crundwell, M.P., Engelmann de Oliveira, C.H., Fagereng, A., Fulton, P.M.,
640 Greve, A., Harris, R.N., Hashimoto, Y., Hüpers, A., Ikari, M.J., Ito, Y., Kitajima, H.,
641 Kutterolf, S., Lee, H., Li, X., Luo, M., Malie, P.R., Meneghini, F., Morgan, J.K., Noda,
642 A., Rabinowitz, H.S., Savage, H.M., Shepherd, C.L., Shreedharan, S., Solomon, E.A.,
643 Underwood, M.B., Wang, M., Woodhouse, A.D., Bourlange, S.M., Brunet, M.M.Y.,
644 Cardona, S., Clennell, M.B., Cook, A.E., Dugan, B., Elger, J., Gamboa, D.,
645 Georgiopoulou, A., Han, S., Heeschen, K.U., Hu, G., Kim, G.Y., Koge, H., Machado,
646 K.S., McNamara, D.D., Moore, G.F., Mountjoy, J.J., Nole, M.A., Owari, S., Paganoni,
647 M., Rose, P.S., Screaton, E.J., Shankar, U., Torres, M.E., Wang, X., and Wu, H.-Y.
648 (2019). Expedition 372B/375 methods. In Wallace, L.M., Saffer, D.M., Barnes, P.M.,
649 Pecher, I.A., Petronotis, K.E., LeVay, L.J., and the Expedition 372/375 Scientists,

650 Hikurangi Subduction Margin Coring, Logging, and Observatories. Proceedings of the
651 International Ocean Discovery Program, 372B/375: College Station, TX (International
652 Ocean Discovery Program). https://doi.org/10.14379/iodp.proc.372B375.102.2019

653 Wang, K., and Bilek, S.L. (2014). Invited review paper: Fault creep caused by
654 subduction of rough seafloor relief. Tectonophysics, v. 610, p. 1–24,
655 https://doi.org/10.1016/j.tecto.2013.11.024.

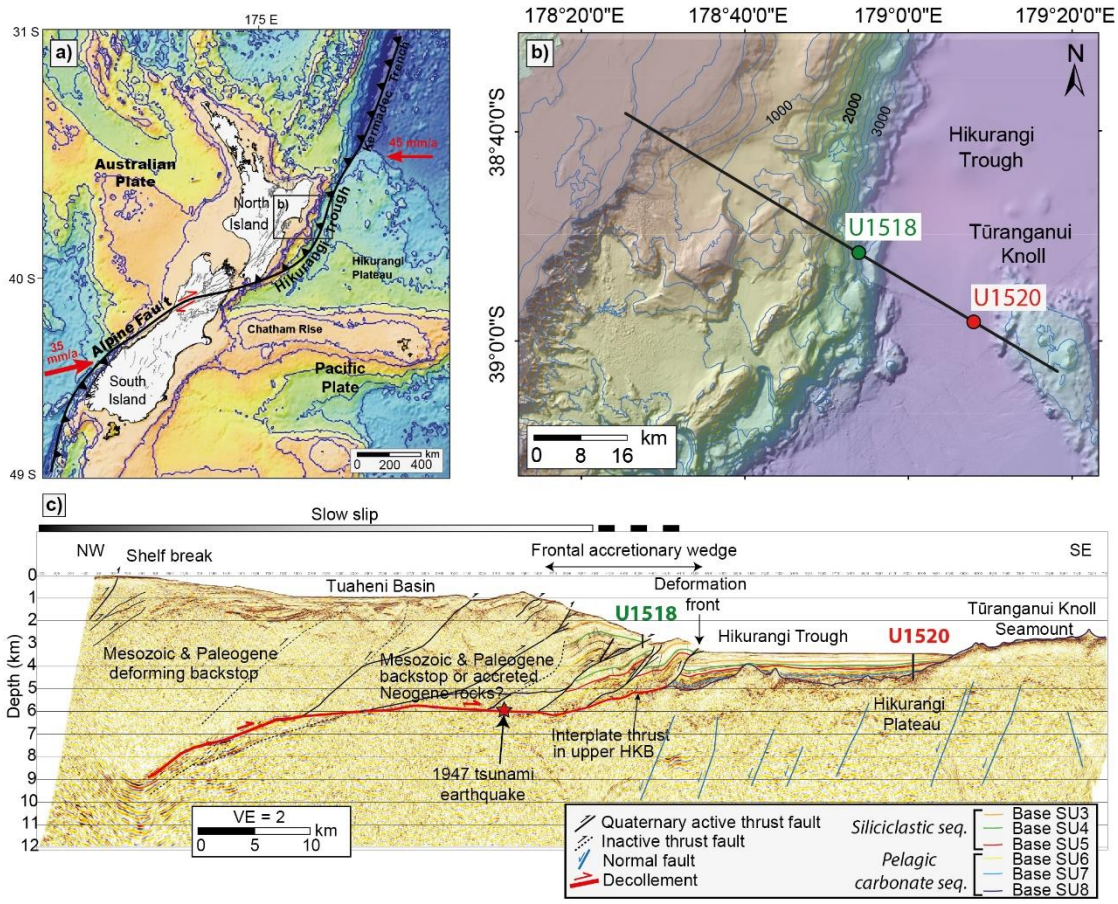

Figure 1. a) Tectonic setting of the Hikurangi margin with plate motion indicated by red arrows. b) bathymetric map of the IODP Expeditions 372/375 study area offshore Gisborne located on a). The black line represents c) the seismic profile 05CM-04 across the margin with main seismic reflectors and structures interpreted from the seismic (Barnes et al., 2020; Fagereng et al., 2019). The red star shows the projected location of March 1947 tsunami earthquake and VE means vertical exaggeration. a), b) and c) are modified from Wallace et al., 2019.

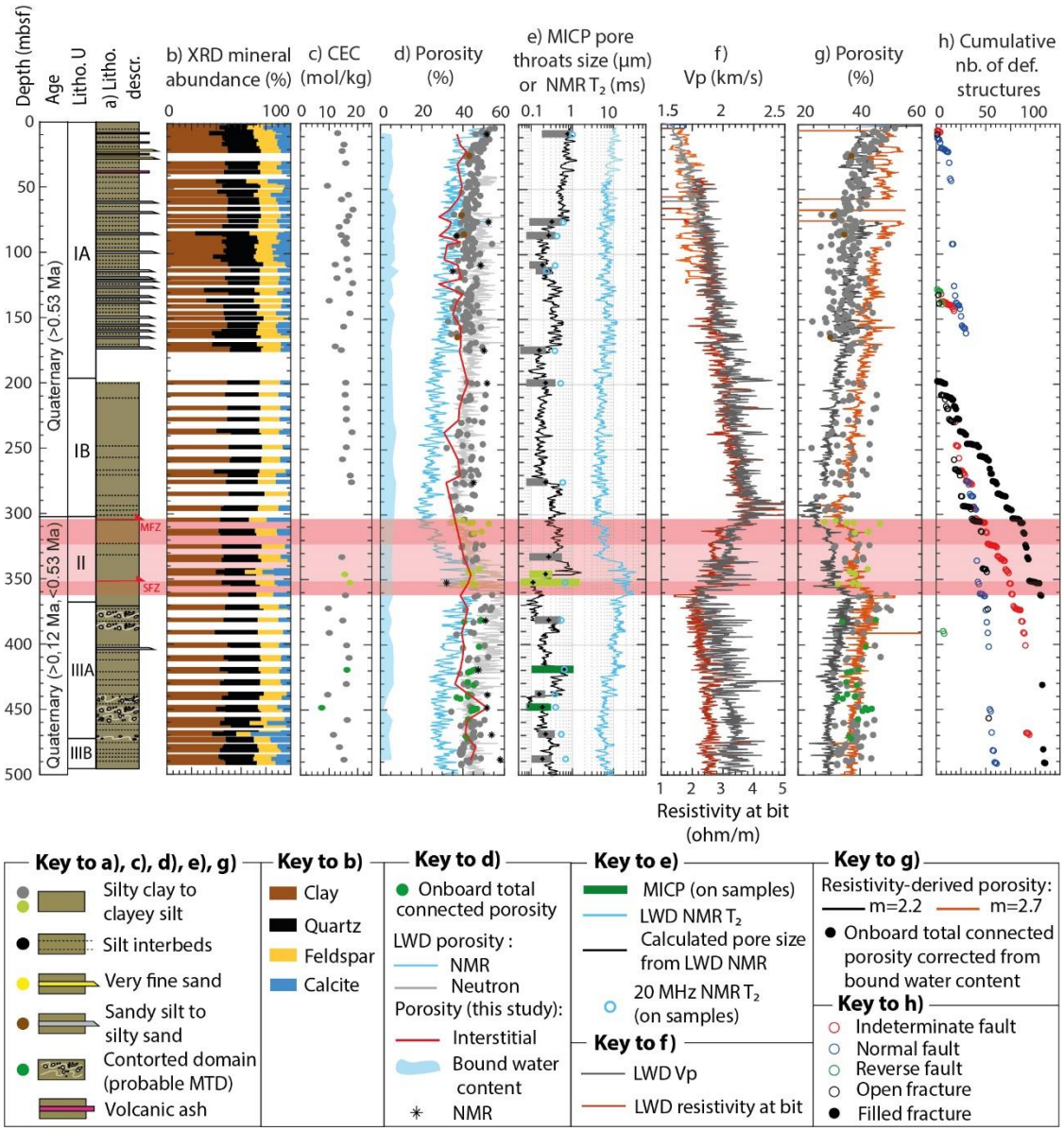

664

665 Figure 2. Lithological units, age and description (a) modified after Wallace et al., 2019
666 mineralogy from onboard XRD (b), cation exchange capacity (c), porosity (d; g), pore
667 structure (e; MICP bars represent pore throat diameters corresponding to at least 40% of
668 the maximal mercury injection, the black star corresponds to average pore throats
669 diameter), (f) LWD resistivity at bit and P-wave velocity (Vp) and deformation
670 structures (h) at Site U1518. The colors of the data points in c), d), e) and g) and MICP
671 bars in e) indicates lithology as reported in the first column. The red shaded zone
672 corresponds to the Pāpaku fault zone with the main fault zone (MFZ from 304 to 322
673 mbsf) and subsidiary fault zone (SFZ from 351 to 361 mbsf). LWD data at hole
674 U1518B were shifted from an average value of -12 mbsf to fit core data following

675 Saffer et al., 2019. For e) and f) LWD data, lighter colors correspond to hole U1518A,
676 darker colors to hole U1518B.

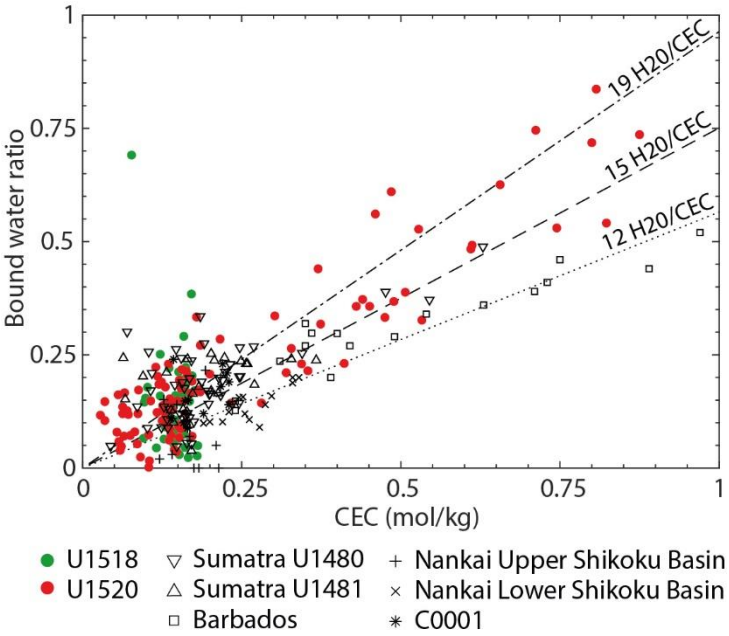

677

678 Figure 3. Volume of chloride-free fluid per volume of grain (bound water ratio) versus
679 cation exchange capacity at North Hikurangi margin Sites U1518 and U1520 (after
680 Dutilleul et al., in press). Theoretical trends are from Henry and Bourlange (2004) and
681 Conin et al. (2011) and correspond to ideal two (resp. three) water layers smectite
682 containing 12, 15 (resp. 19) water molecules per cation charge (Henry, 1997). Data for
683 Sumatra are from Dutilleul et al. (2020), Barbardos are from Henry (1997), Nankai
684 Upper and Lower Shikoku Basin are from Henry and Bourlange (2004) and Site C0001
685 are from Conin et al. (2011).

686

Figure 4. Relations between pore structure and porosity at Site U1518 (green) in the hanging-wall, the fault zone and the upper footwall and in siliciclastic Units I-III from reference Site U1520 (red) (after Dutilleul et al., in press). a) Relation between mean pore throats diameter and mercury trapped porosity. b) Relation between mean pore throats diameter and interstitial porosity. c) Relation between interstitial porosity and mercury porosity (open circles) or mercury trapped porosity (circles). Trends were determined using the least square method.

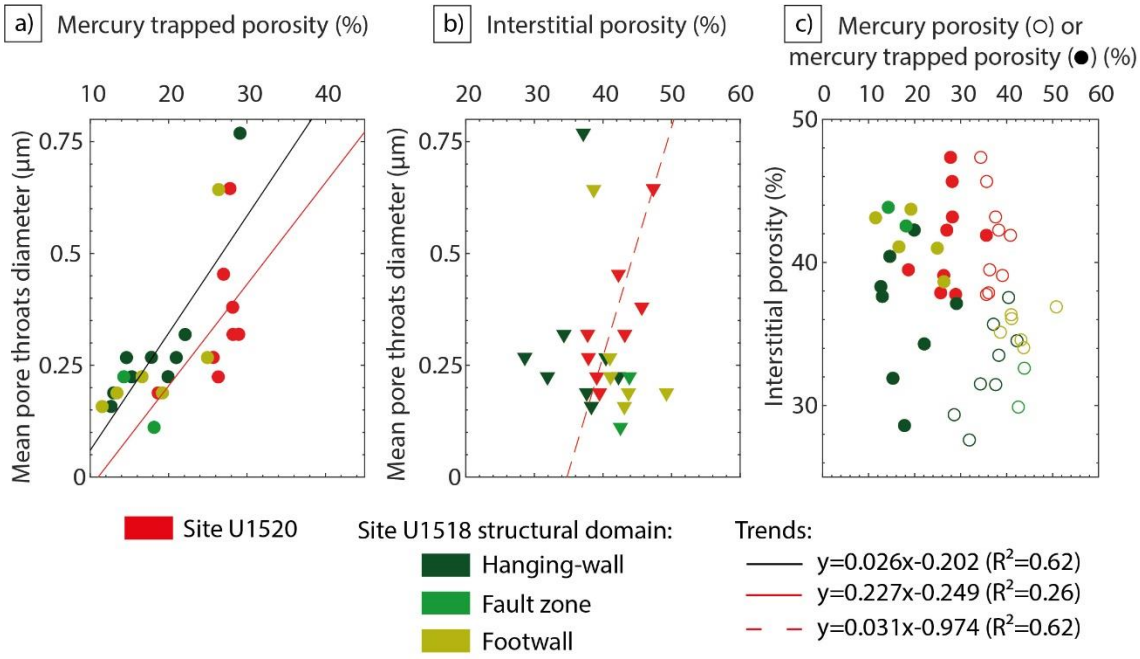

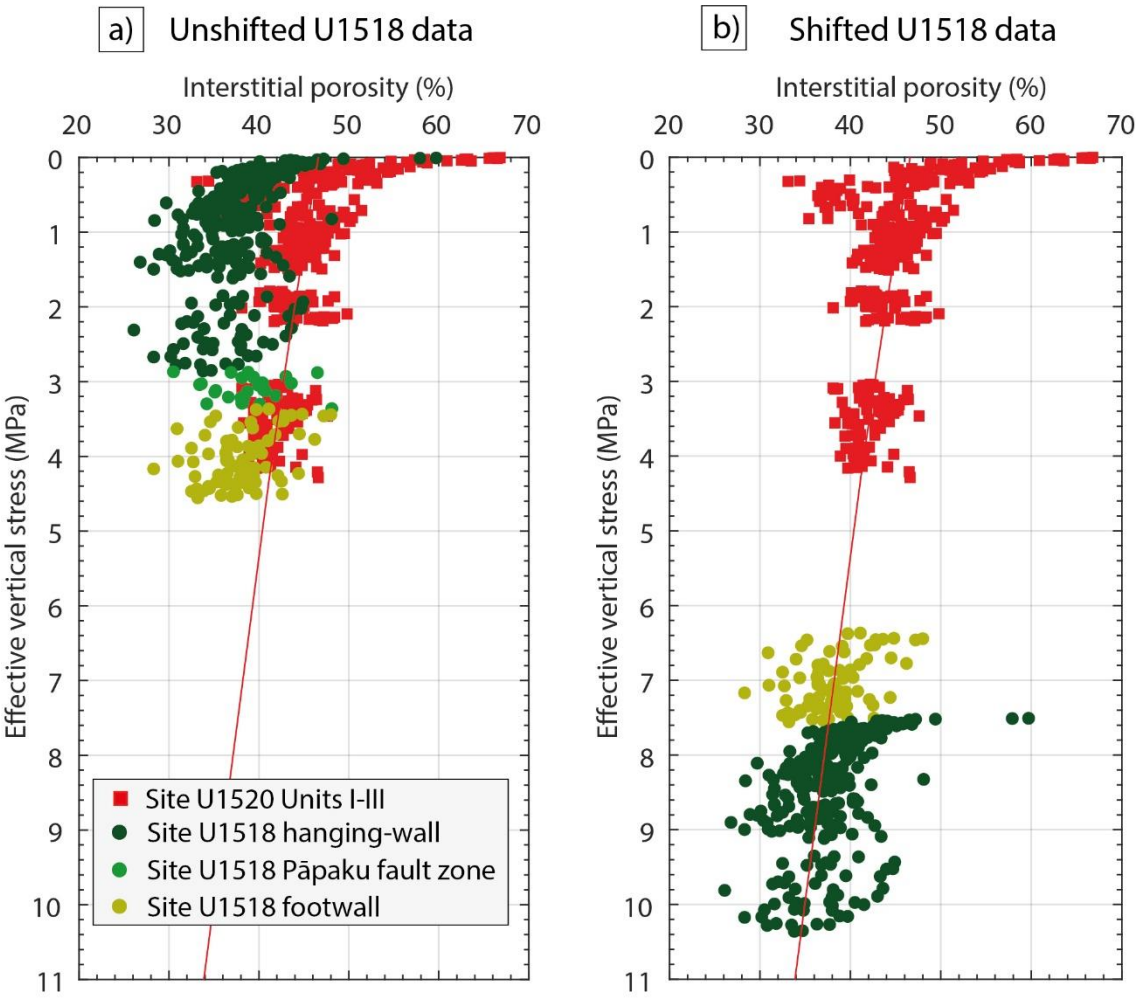

Figure 5. a) Comparison of interstitial porosity data at Site U1518 (green) and reference Site U1520 (red), with reference compaction trend $\phi_i = 46.6e^{-0.029\,\sigma'_v}$ (R^2=0.29) (red line) corresponding to Site U1520 siliciclastic Units I to III, sand-rich and very shallow unconsolidated samples excluded. b) Vertical effective stress shifts to fit interstitial porosity data of Pāpaku thrust hanging-wall (dark green, +7.5 MPa or ~830 mbsf) and footwall (light green, +3.0 MPa or ~330 mbsf) to the reference compaction curve.

Figure 6. Comparison of a) MICP pore throats size distribution, b) main pore throats diameters, c) NMR T_2, and d) Katz-Thompson permeability K_{KT} of samples from Site U1518 (green) and Site U1520 (red) siliciclastic Units I-III (Dutilleul et al., in press). The red PFZ zone corresponds to the Pāpaku fault zone at Site U1518 (~301-361 mbsf).

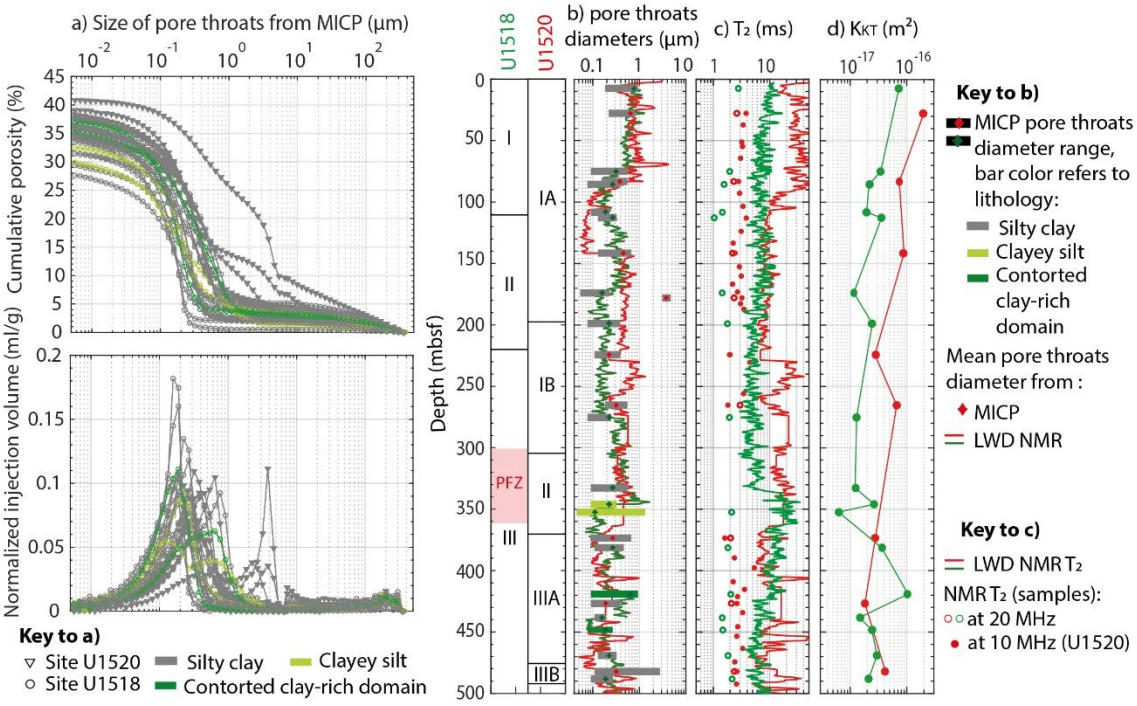

Figure 7. Tectonic (a, b, c) or hydrologic (d) events affecting interstitial porosity-vertical effective stress pattern.

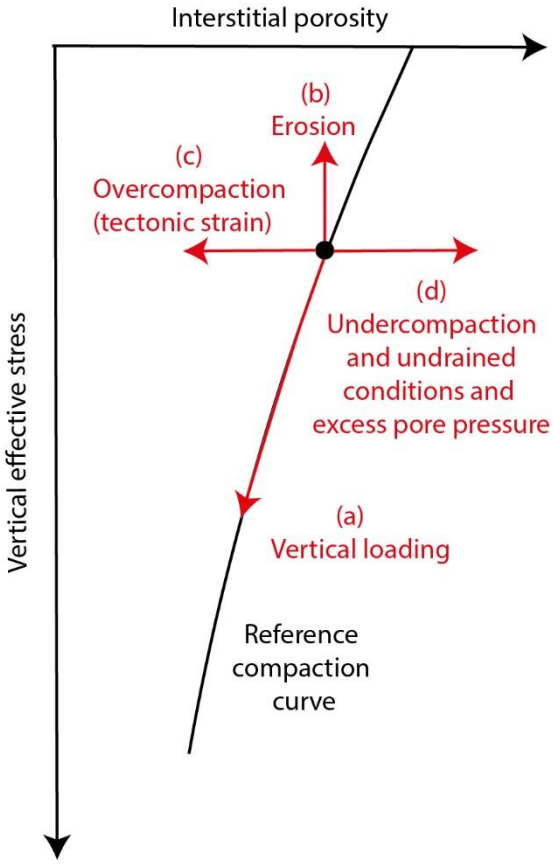

Figure 8. Schematic deformation and erosion history at Site U1518, with a) normal consolidation of the hanging-wall (HW) and the footwall (FW) in the entering basin; b) thrusting of the hanging-wall above the footwall concomitant with ~500 meters of erosion and c) supplementary erosion of ~330 meters of the hanging-wall once it is set above the footwall to finally reach present setting.

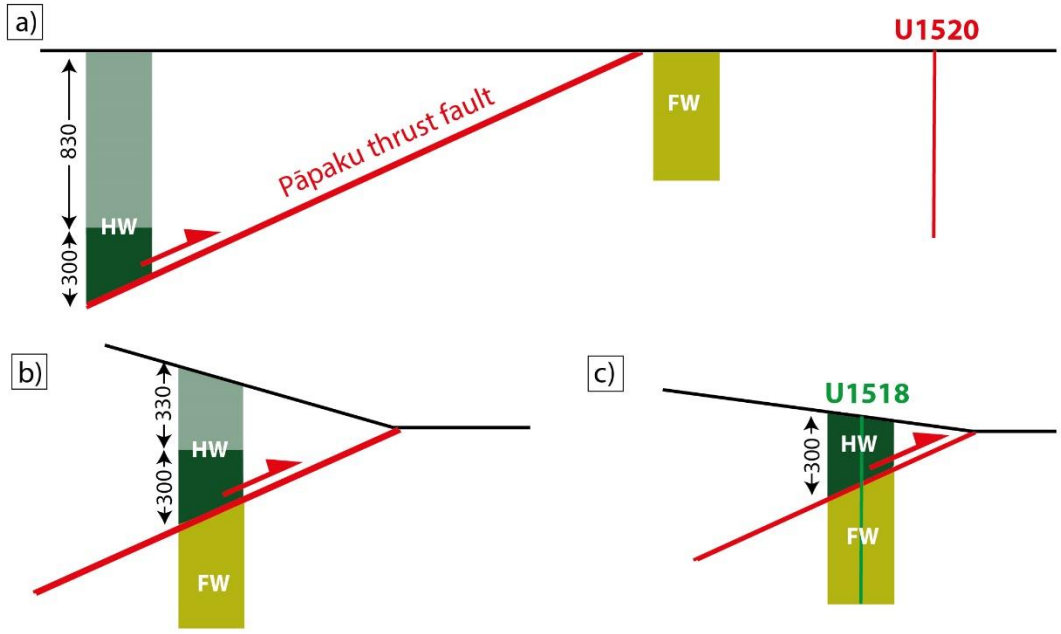

Type of porosity\Zone	Entire sequence	Hanging-wall	Footwall
a) Total connected porosity ϕ_t	a=44.3 b=0.008275 R²=0.00176	a=45.83 b=0.04986 R²=0.12	a=51.34 b=0.04073 R²=0.06421
b) Interstitial porosity ϕ_i	a=38.25 b=0.008782 R²=0.009	a =40.59 b=0.08071 R²=0.1778	a =42.71 b=0.02892 R²=0.0204

Table 1. Parameters for the relation $\phi_{i\,or\,t} = ae^{-b\,\sigma_v'}$ describing the exponential decrease of a) onboard total connected porosity (ϕ_t) and b) interstitial porosity (i.e: ϕ_i onboard total connected porosity corrected from average bound water content) with increasing effective vertical stress (σ_v') in the entire sedimentary section, the hanging-wall only or the footwall only at Site U1518. Parameters are determined using the least square method.

Figure1.

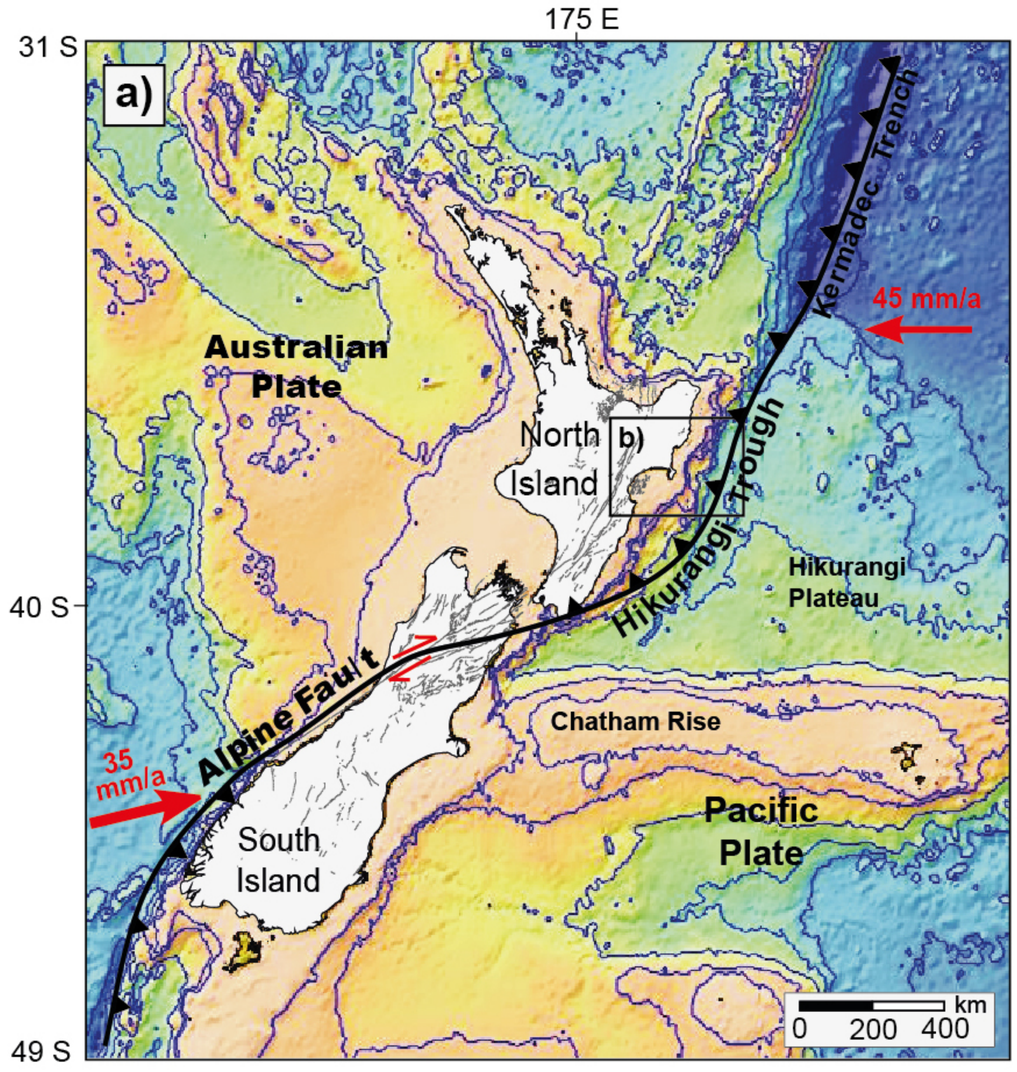
a)
175 E
31 S
40 S
49 S
Australian Plate
North Island
b)
South Island
Kermadec Trench
Hikurangi Trough
Hikurangi Plateau
Chatham Rise
Pacific Plate
Alpine Fault
45 mm/a
35 mm/a
km
0 200 400

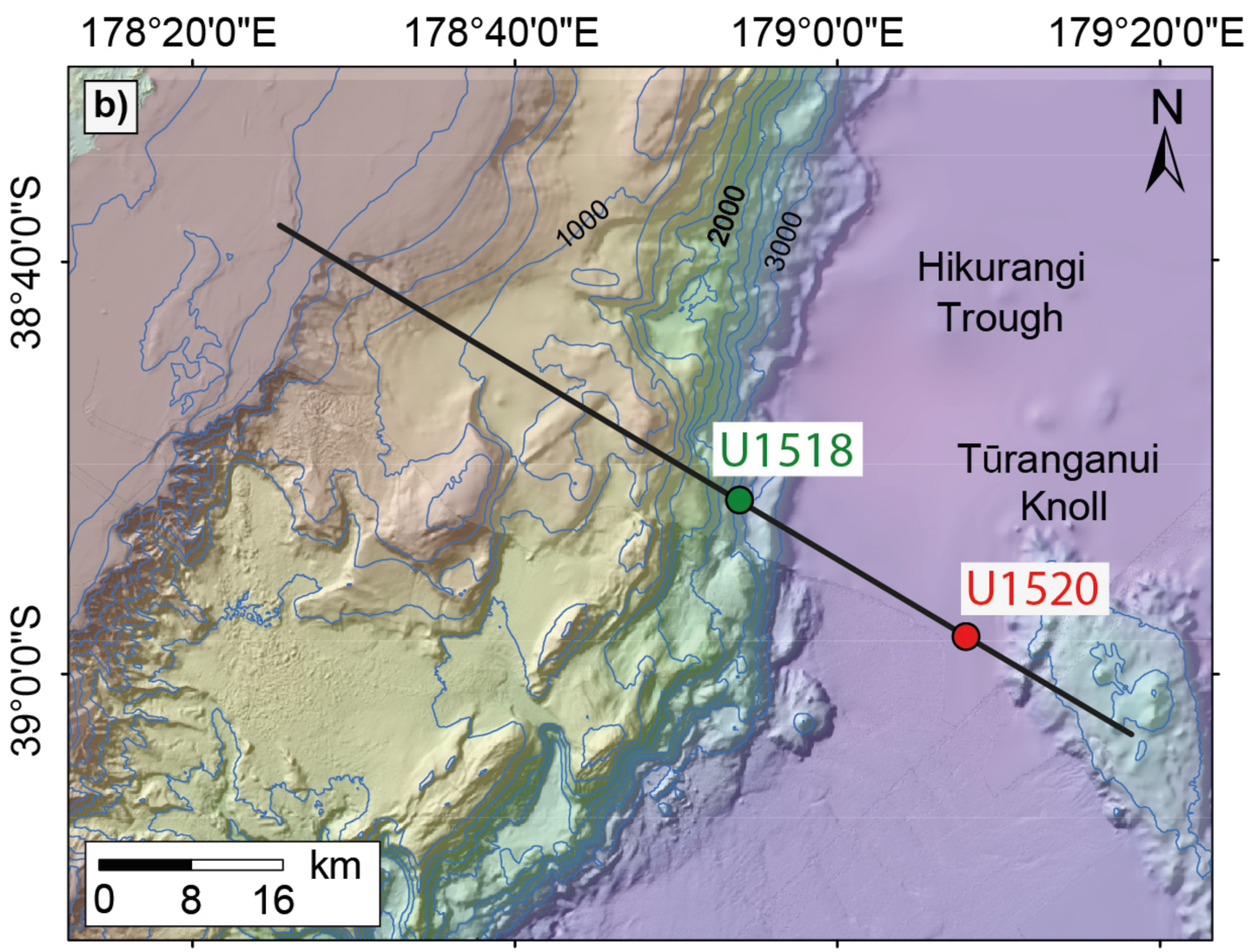
b)
N
178°20'0"E
178°40'0"E
179°0'0"E
179°20'0"E
38°40'0"S
39°0'0"S
1000
2000
3000
Hikurangi Trough
U1518
Tūranganui Knoll
U1520
km
0 8 16

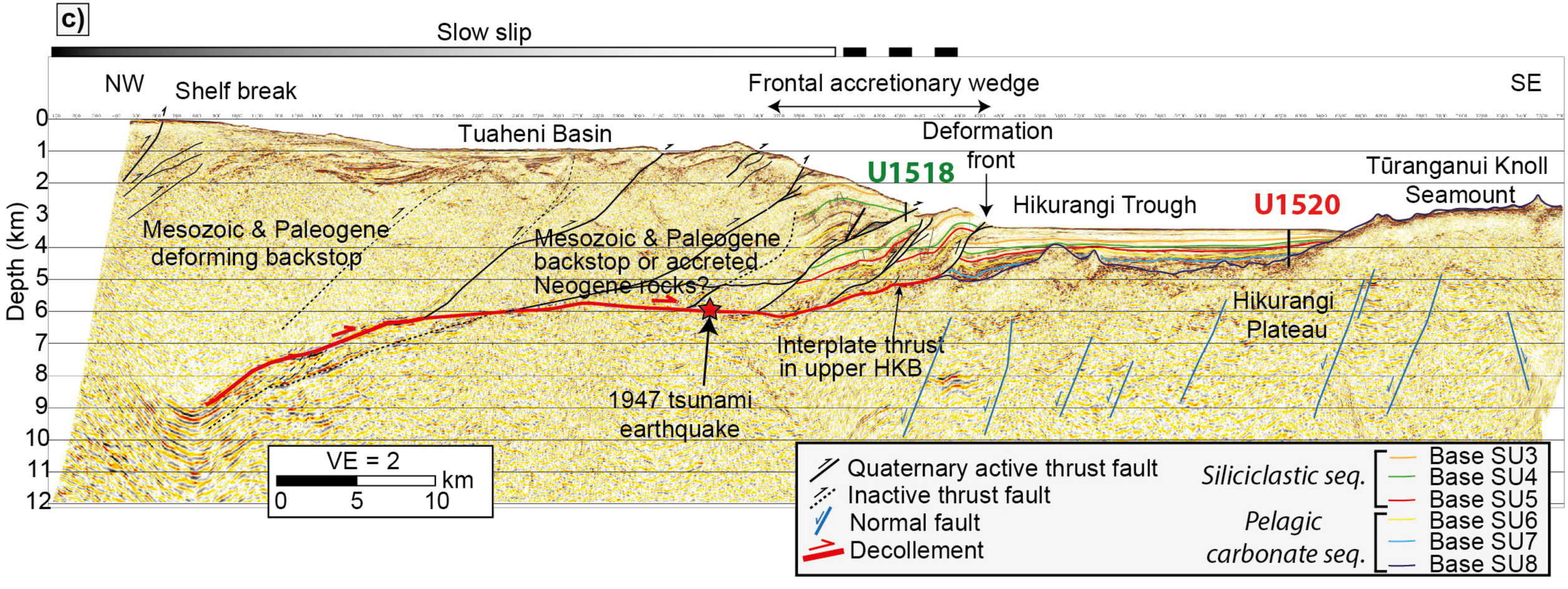
c)
Slow slip
NW
SE
Shelf break
Tuaheni Basin
Frontal accretionary wedge
Deformation front
U1518
U1520
Tūranganui Knoll Seamount
Hikurangi Trough
Hikurangi Plateau
Mesozoic & Paleogene deforming backstop
Mesozoic & Paleogene backstop or accreted Neogene rocks?
Interplate thrust in upper HKB
1947 tsunami earthquake
Depth (km)
0
1
2
3
4
5
6
7
8
9
10
11
12
VE = 2
km
0 5 10
Quaternary active thrust fault
Inactive thrust fault
Normal fault
Decollement
Siliciclastic seq.
Pelagic carbonate seq.
Base SU3
Base SU4
Base SU5
Base SU6
Base SU7
Base SU8

Figure2.

Depth (mbsf)
Age
Litho. U
a) Litho. descr.
b) XRD mineral abundance (%)
c) CEC (mol/kg)
d) Porosity (%)
e) MICP pore throats size (µm) or NMR T_2 (ms)
f) Vp (km/s)
g) Porosity (%)
h) Cumulative nb. of def. structures

0 100
0 10 20
0 20 40 60
0.1 1 10
1.5 2 2.5
20 40 60
0 50 100

0
50
100
150
200
250
300
350
400
450
500

Quaternary (>0,53 Ma)
IA
IB
II
Quaternary (>0,12 Ma, <0.53 Ma)
IIIA
IIIB
MFZ
SFZ

1 2 3 4 5
Resistivity at bit (ohm/m)

Key to a), c), d), e), g)

- Silty clay to clayey silt
- Silt interbeds
- Very fine sand
- Sandy silt to silty sand
- Contorted domain (probable MTD)
- Volcanic ash

Key to b)

- Clay
- Quartz
- Feldspar
- Calcite

Key to d)

- Onboard total connected porosity

LWD porosity :
- NMR
- Neutron

Porosity (this study):
- Interstitial
- Bound water content
- NMR

Key to e)

- MICP (on samples)
- LWD NMR T_2
- Calculated pore size from LWD NMR
- 20 MHz NMR T_2 (on samples)

Key to f)

- LWD Vp
- LWD resistivity at bit

Key to g)

Resistivity-derived porosity:
- m=2.2
- m=2.7
- Onboard total connected porosity corrected from bound water content

Key to h)

- Indeterminate fault
- Normal fault
- Reverse fault
- Open fracture
- Filled fracture

Figure2.

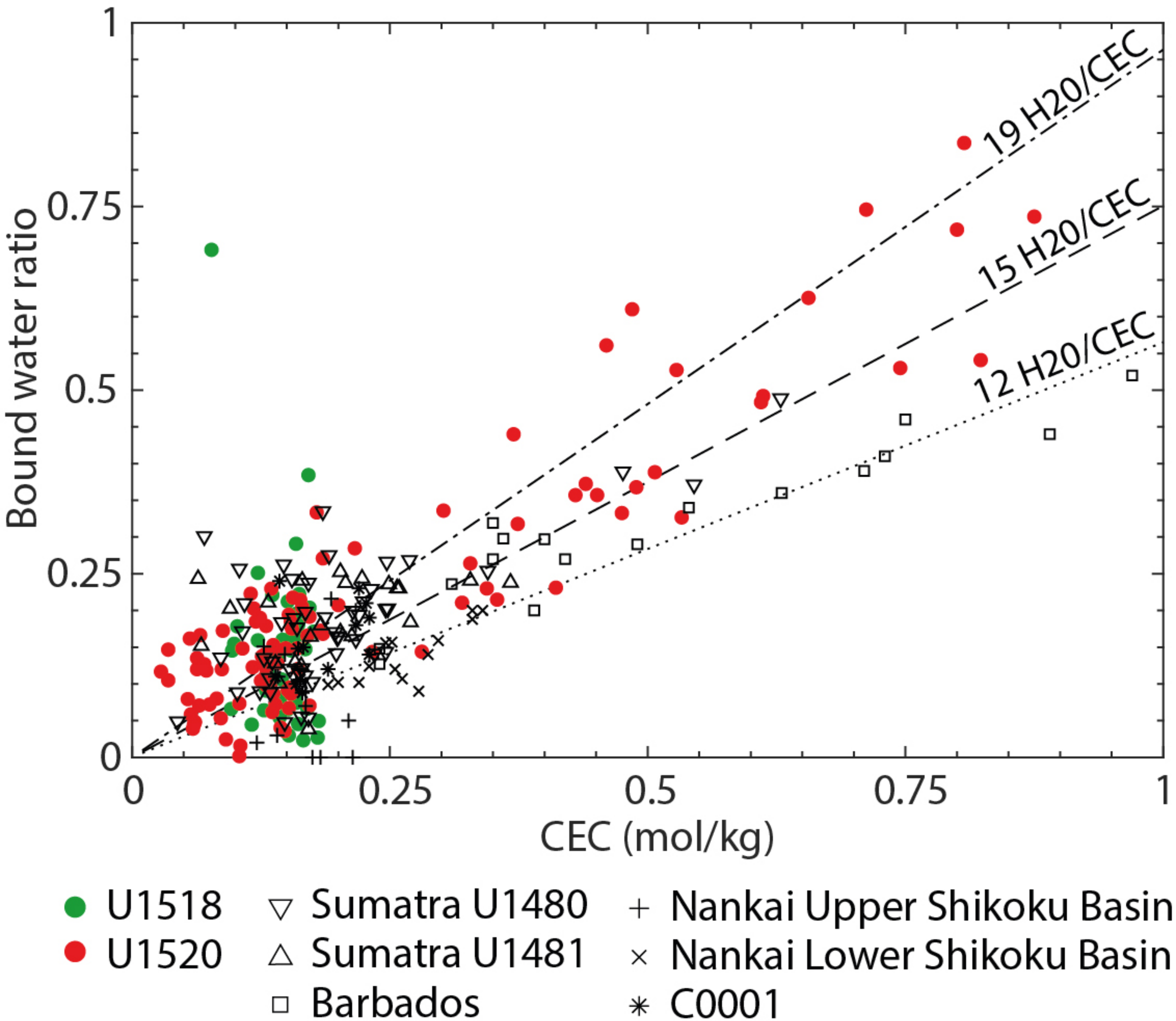
Bound water ratio
CEC (mol/kg)
0
0.25
0.5
0.75
1
19 H20/CEC
15 H20/CEC
12 H20/CEC
U1518
U1520
Sumatra U1480
Sumatra U1481
Barbados
Nankai Upper Shikoku Basin
Nankai Lower Shikoku Basin
C0001

Figure4.

a) Mercury trapped porosity (%)

b) Interstitial porosity (%)

c) Mercury porosity (○) or mercury trapped porosity (●) (%)

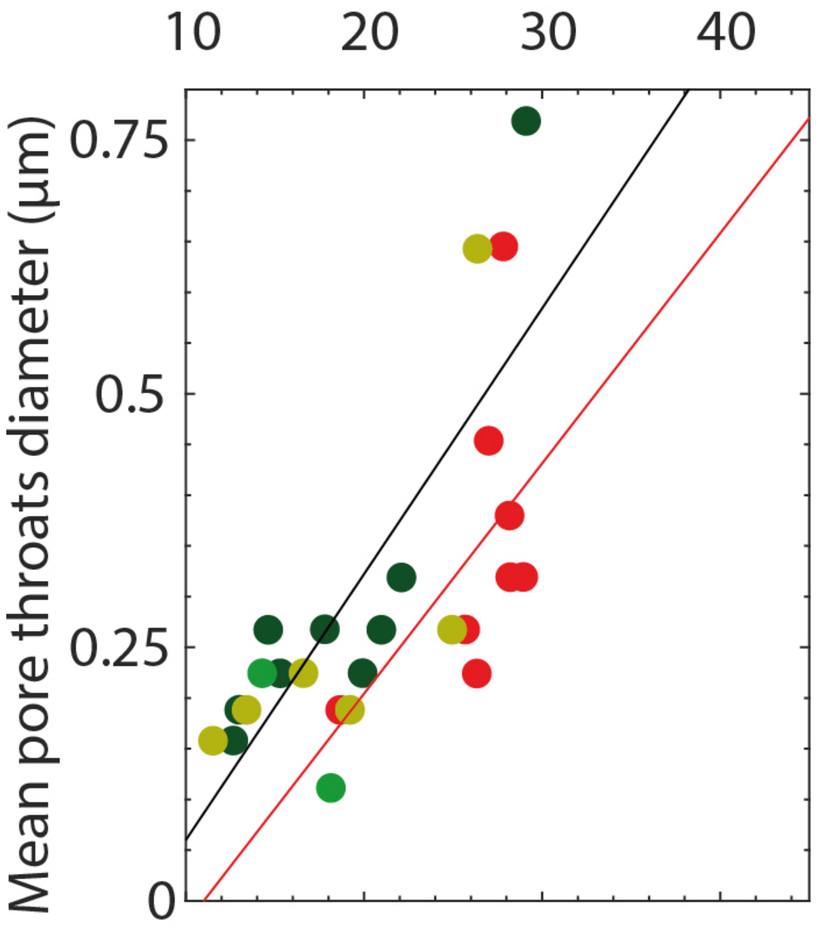

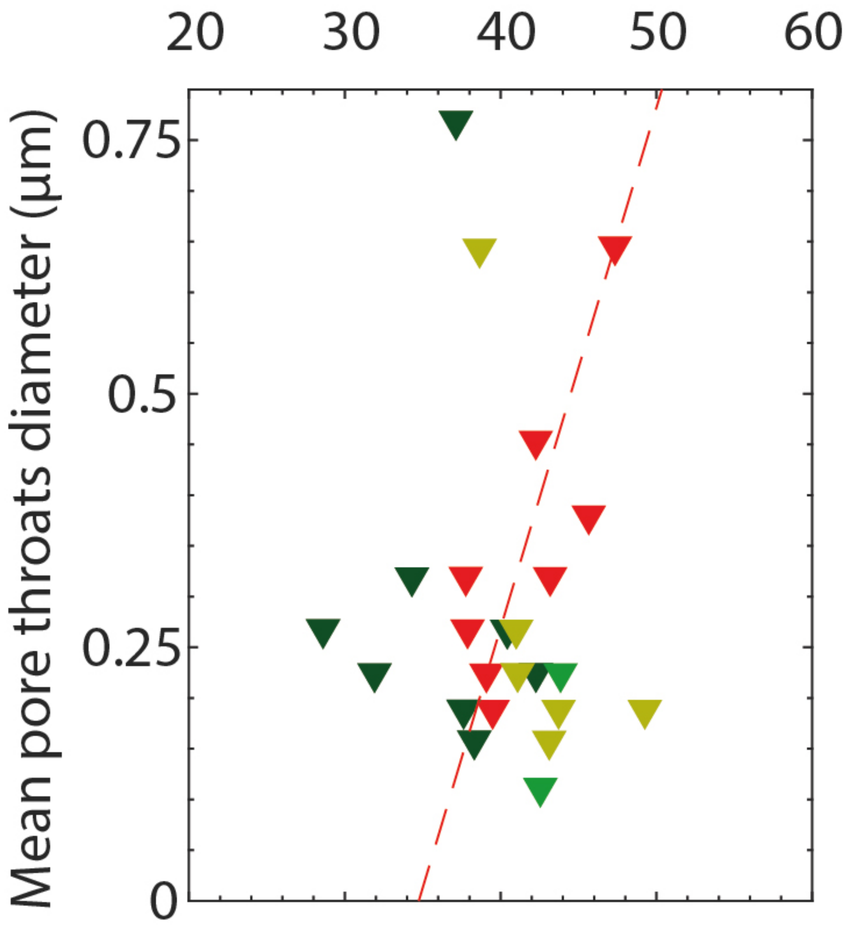

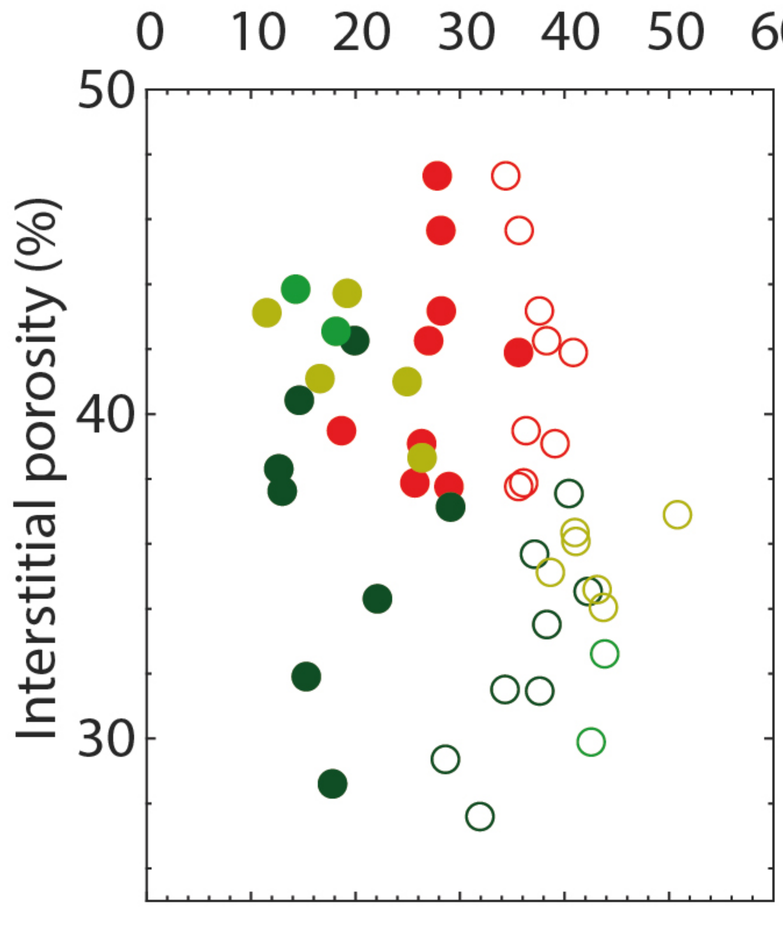

Site U1520

Site U1518 structural domain:

- Hanging-wall
- Fault zone
- Footwall

Trends:

- y=0.026x-0.202 (R^2=0.62)
- y=0.227x-0.249 (R^2=0.26)
- y=0.031x-0.974 (R^2=0.62)

Figure5.

a) Unshifted U1518 data

b) Shifted U1518 data

Interstitial porosity (%)

20 30 40 50 60 70

0 1 2 3 4 5 6 7 8 9 10 11

Effective vertical stress (MPa)

Site U1520 Units I-III
Site U1518 hanging-wall
Site U1518 Pāpaku fault zone
Site U1518 footwall

Figure6.

a) Size of pore throats from MICP (µm)

Cumulative porosity (%)

Normalized injection volume (ml/g)

Key to a)

- ▽ Site U1520
- ○ Site U1518
- Silty clay
- Clayey silt
- Contorted clay-rich domain

U1518 U1520

b) pore throats diameters (µm)

c) T_2 (ms)

d) K_{KT} (m^2)

Depth (mbsf)

I, IA, II, IB, PFZ, II, III, IIIA, IIIB

Key to b)

- MICP pore throats diameter range, bar color refers to lithology:
  - Silty clay
  - Clayey silt
  - Contorted clay-rich domain

Mean pore throats diameter from :

- MICP
- LWD NMR

Key to c)

- LWD NMR T_2

NMR T_2 (samples):

- ○ at 20 MHz
- ● at 10 MHz (U1520)

Figure7.

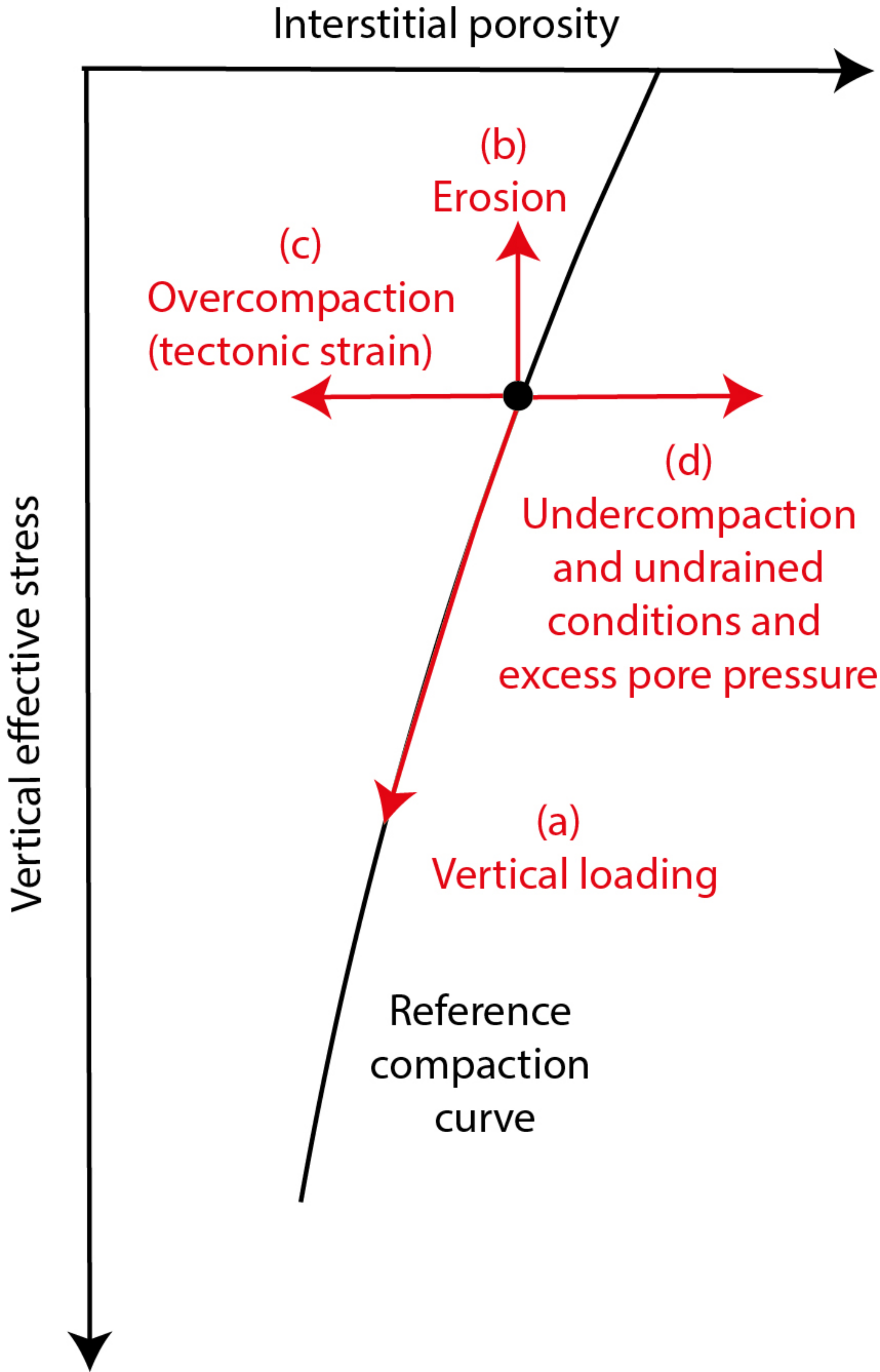
Interstitial porosity
Vertical effective stress
(b)
Erosion
(c)
Overcompaction
(tectonic strain)
(d)
Undercompaction
and undrained
conditions and
excess pore pressure
(a)
Vertical loading
Reference
compaction
curve

Figure8.

a)

U1520

830

300

HW

Pāpaku thrust fault

FW

b)

330

300

HW

FW

c)

U1518

300

HW

FW